Investigating the Aerodynamic Performance of Biomimetic Gliders for Use in Future Transportation

Authors: Wang Jiwei, Wang Yiyang, Zhang Haoyu

Advisors: Dr. Victor Wang Peng Cheng, Mr. Khoh Rong Lun

Institutes: Temasek Junior College & Anglo-Chinese Junior College

Country: Singapore

Abstract:

Personal flying vehicles have the potential to solve many of our traffic problems such as congestion, due to their ability to travel at different heights. This would in turn allow for better land use. As such, they are becoming increasingly relevant in today's world. The study presented in this paper aims to contribute to this field by identifying structures that are ideal for the use of future traffic. This study focuses on the concept of biomimicry, looking to nature's best flyers and gliders and comparing the flight performances of the structures of these species. Though there have been studies investigating flying species and their structures, none have broadly discussed and compared their performances. The ten species were modelled then analysed by both XFOIL method and high fidelity ANSYS Fluent simulation in the form of Computational Fluid Dynamics (CFD). Of the ten species analysed and compared aerodynamically, the best two wing species were then 3D printed and tested in an open return wind tunnel. Detailed analysis suggested that the structure of the Javan Cucumber was superior in terms of flight performance. In addition, this model was refined in XFLR5 and applied to a full-scale model which was further analysed in ANSYS Fluent. The comparison between Javan Cucumber and current commercially available powered glider design, XT912 Tundra-Merlin, shown the advantage of such design and its potential to be further studied in the future. In addition, the Javan Cucumber model was prototyped by Computer Numerical Control (CNC) and installed on a Micro Air Vehicle (MAV) platform. Following flights of the prototype have suggested its excellence in terms of flying capability.

Key Words:

Biomimicry, Aerodynamics, Glider, XFOIL, CFD, ANSYS Fluent, Javan Cucumber, CNC, MAV

Innovation Statements

The paper submitted contains the research results we have obtained under the guidance of our advisors. To the best of our knowledge, this paper does not incorporate any research result that have been published or written by other people or teams, unless specifically noted and acknowledged in the text. If there is any dishonesty, we are willing to bear all the relevant responsibilities.

Team members： Wang Jiwei, Wang Yiyang, Zhang Haoyu

Content

Nomenclature:

Symbols	Name of Quantities	Units
CD	drag coefficient	
CL	lift coefficient	
CL/CD	lift coefficient to drag coefficient ratio	
L	lift force	N
D	drag force	N
Re	Reynolds number	
ρ	density	$kg\cdot m^{-3}$
α	angle of attack	°
μ	dynamic viscosity	$\frac{N\cdot s}{m^2}$
x	length of the panel	m
V	airspeed	m/s
Γ	vortex strength	
S	planform area	m^2
t	time	s
p	pressure	Pa
Et	total energy	J

Acronyms:

Acronyms	Full Terms
AC	Aerodynamic Centre
AoA	Angle of Attack
AR	Aspect Ratio
BC	Boundary Condition
CAD	Computational Aided Drawing
CFD	Computational Fluid Dynamics
CNC	Computer Numerical Control
CP	Centre of Pressure
EPP	Expanded Polypropylene
FDM	Fused Deposition Modelling
LLT	Lifting Line Theory
LRN	Low Reynolds Number
MAC	Mean Aerodynamic Chord
MAV	Micro Air Vehicle
MRT	Mass Rapid Transit
PLA	Polylactic Acid
RANS	Reynolds-Averaged Navier-Stokes equations
SIMPLE	Semi-Implicit Method for Pressure Linked Equations
SIMPLEC	Semi-Implicit Method for Pressure Linked Equations-Consistent
TM	Turbulence Model
VLM	Vortex lattice method

I. Introduction

A. Background

Congestions and its introduced time loss have long been regarded as major issues in modern lives. To address these issues, the utilisation of short-range air transportation has been proposed. Unlike land transport, flying vehicles can allow for better use of the air space instead of relying on limited land area. Personal flying vehicles can then help in reducing congestion as commuters can fly at different heights and even use routes that would otherwise be inaccessible by road.

B. Literature Review, Research Aim and Criteria for Selection

Personal flying vehicles have long been a staple of science fiction and imagination. In reality, companies such as Uber are already working on flying cars which are set to be completed by 2020 [1]. However, apart from flying cars, there are also other flying vehicles that are currently already in use but can be further improved [2]. One such vehicle is the powered glider, which requires less distance to take off and land, can take 1 to 2 people and use gliding as its primary power source [3]. Currently, it is widely used as a sport activity, especially in the United States and Australia. Although it has been used for many years, its overall structure has remained mostly unchanged. Thus, there are spaces for it to be improved so that it can also be used in future transportation. Biomimicry has been long applied in aircraft design [4]; however, these aircrafts usually have a tiny load capacity [5], or there has not been a broad comparison across species to discover which offers the best structure for flight [6][7].

In the glider designing, engineers mainly regard the high CL/CD and low sink rate as two criteria for better models. Considering the carrying ability of planes, the commercial aircraft industries usually place the lift as an indication of aircrafts' performance. In this research, the new powered gliders were designed for transportation. This usage would require flights with high efficiency and glide for long distance with high loads, coinciding with the glider designers' and commercial aircraft designers' considerations.

For both high efficiency and long distance, the models should have a high CL/CD under a large range of Angle of Attacks (AoA). Taking the glide theories in Fig.1 into consideration, the CL/CD is equal to the L/D ratio. From Fig.1, it is observed that the angle between the lift L and the overall aerodynamic force R, is equal to the glide angle α. Thus, the CL/CD = L/D = 1/tan(α) = d/h, where d is the horizontal distance and h is the vertical distance. This equation suggests that the ratio of distance travelled to height loss is equal to the CL/CD ratio. Therefore, a higher CL/CD will result in a larger distance/height ratio, which suggests that the model can travel a longer distance when gliding down the same height. This model is thus more efficient. However, it is not sufficient to have a high CL/CD ratio at a single AoA, as the actual glide angle is subject to frequent change of wind, temperature and pressure changes. Thus, the best performing species should have large CL/CD ratios in a broad range of AoAs.

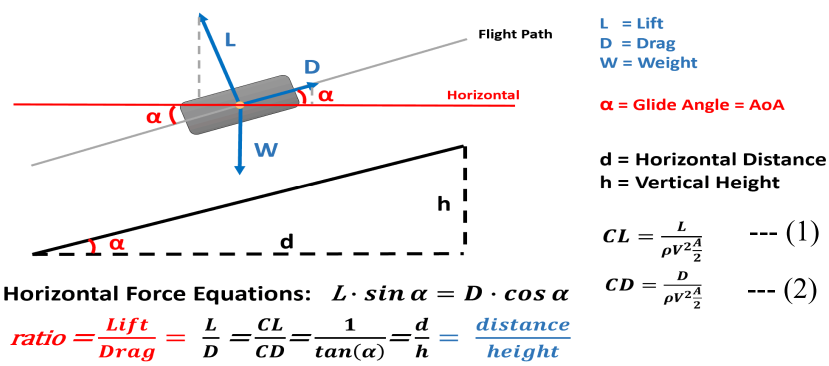

Figure 1. Graphical illustration of the CL/CD in glide theory.

The sink rate quantified by CL^1.5/CD, however, was not one of our criteria. This is because the flight at the lowest sink rate will not glide the farthest, as the minimum sink rate requires the aircraft to glide at a higher CL but lower speed. Thus, the glider travels less distance with lower gliding speed, making the range of flight shorter than that of gliding at maximum CL/CD. The criterion of lowest sink rate was thus contradicting to our aim.

To carry high loads, the glider simply needs to generate a relatively large lift under its working conditions. Generally, gliders work under the AoA of 3 to 8 degrees [8]. If the biomimetic designs can generate a large lift in or even broader than this range, its actual carrying ability can thus considered as good.

Overall, the prioritised criterion of our selection for best models is the high CL/CD in a broad range of AoAs. We will later compare the performances by comparing models' CL/CD-AoA graphs. If the model's graph is vertically above others', it can thus sustain a higher CL/CD in any AoA, making it more efficient and glide farther. Its performance will be even better if the lift generated by the model is large. The lift of the model is placed as the secondary criterion as the lift generated by our models is usually large, making it not as important as the CL/CD.

C. Design Methodology

One conventional way of wing design is to apply the theory of control of partial differential equations (J.L.Lions) in conjecture with CFD [9]. In this way, the expected features of the wing, including sweep, dihedral and airfoil etc. can be designed out. Then, CFD analysis is used to test if the performance of the designed wing meets the requirement. Despite the theoretical CFD way, experiments are also usually conducted, mainly to test the performance of the wing in the real world. After all these steps, a new wing design with expected performances finally determined.

D. Adopt Methodology

This research did not utilise the method aforementioned, namely the use of theory of control, to design a new wing. Instead, biomimicry was preferred to be used as an inspiration of the wing design, which means that one of existing wing shapes in nature will be chosen as the final wing design proposed by this research. This is mainly because all these wing designs are nature's time-tested patterns and strategies, which means that they may outperform current man-made wing design that is based on empirical knowledge.

In order to select out the best wing design from the pool of wing shapes in nature, CFD analysis and experiment were both used to test these wings and determine the wing design that has the best performance. Moreover, CFD analysis was further used to compare the performance of the best biomimetic wing designs and the current man-made wing design to justify our selections.

E. Problem Statement

This research seeks to find a better design for powered gliders using biomimicry (the criteria were mentioned in Chapter I.B). These wing designs would have the best aerodynamic performance on gliders by a broad comparison and selection across all flying or gliding species. This research is anticipated to go beyond the theories and make great practical contributions to the developments of personal flying vehicles for future transport.

II. METHODOLOGY

A. Hypothesis

Among all the species to be studied, we hypothesised that the Javan Cucumber would perform the best. The Javan Cucumber features elliptical wings, which was seen in the advanced Spitfire plane during the Second World War. According to Model Aircraft Aerodynamics written by Martin Simons, the elliptical wing produces a constant downwash at any speed with the minimum induced drag for a given lift.

B. Overall Flowchart

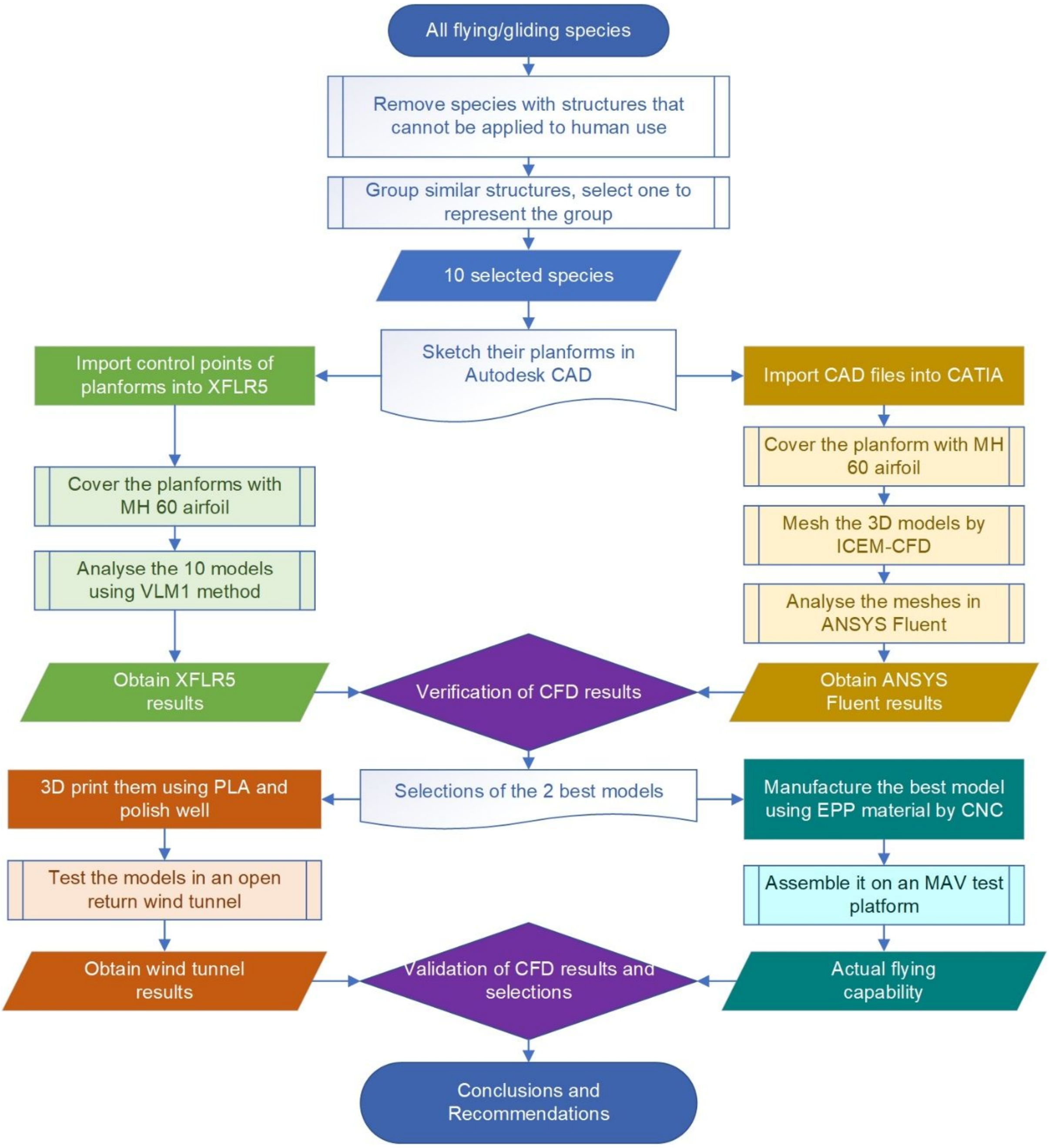

Figure 2. The overview of the implemented methodology

This research is done in 7 steps.

Firstly, we shortlisted the species to study.

Secondly, we scaled all the models to have a wingspan of 30cm which would be convenient for our investigation.

Thirdly, we used Autodesk CAD 2016 to sketch their planforms and imported them into XFLR5. We then did a computational simulation based on XFLR5 to analyse the aerodynamic characteristics and performances of these models.

Fourthly, we constructed the 3D models using CATIA V5 R20, then meshed the models in ICEM-CFD 18.0 and conducted the verification test using ANSYS Fluent 18.0.

Fifthly, the 2 best models are selected, 3D-printed, and tested in an open return wind tunnel to validate the results obtained from the CFD. A pre-validation using standard wing section was conducted before the test to find the accuracy of the wind tunnel.

Sixthly, we chose a reputable commercial model, XT912 Tundra Merlin, to compare and evaluate the performance of the best model.

Lastly, we prototyped the best model using CNC milling and installed it on a MAV to test its flying capability.

C. Selection of Species

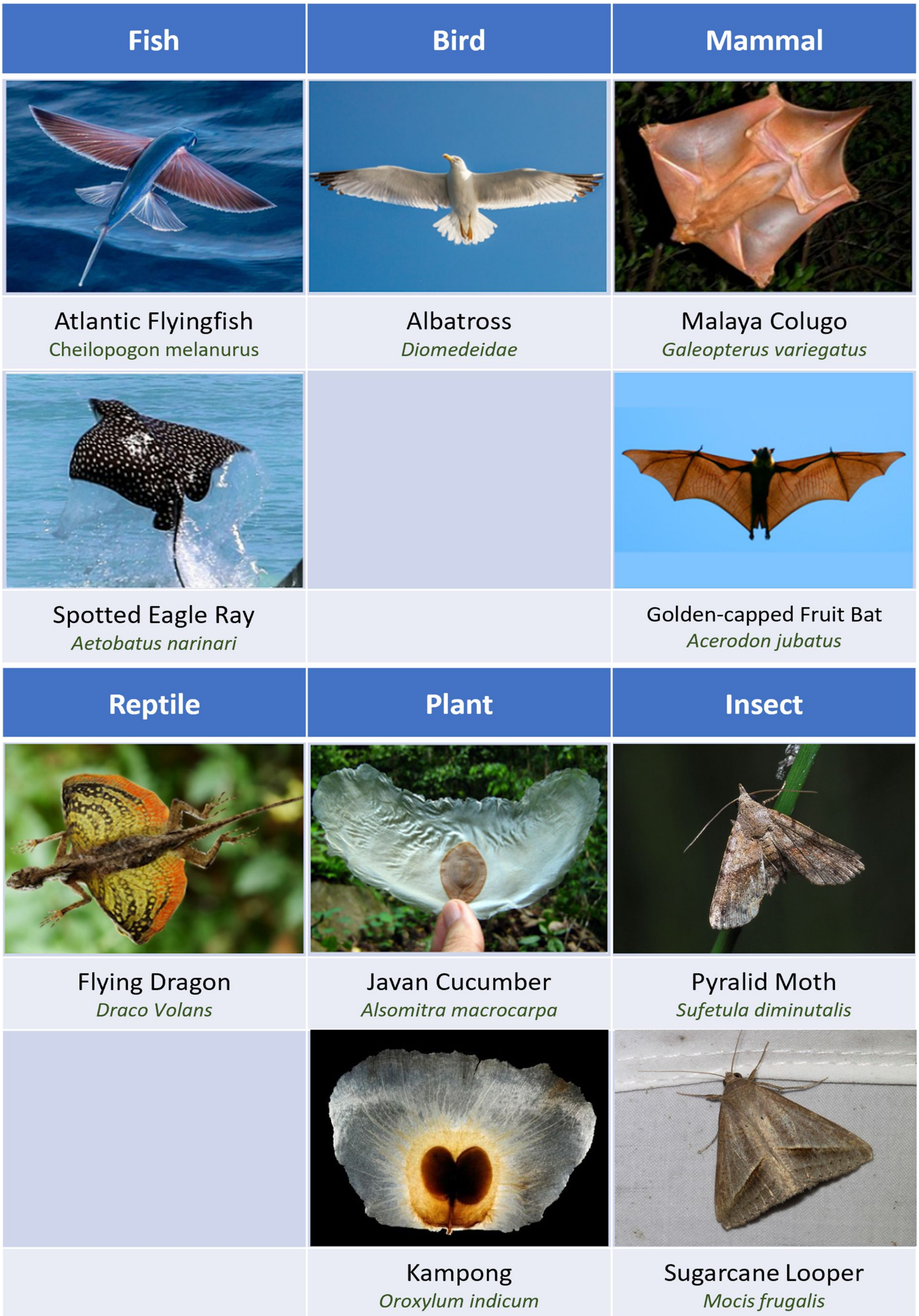

Figure 3. Ten different species selected.

The species were chosen such that they allowed us to broadly cover most types of flying species in nature, allowing us identify which type of flying species has the best structure that we can apply to powered gliders. The process of choosing the species to study can be divided into three phases. In the first phase, we shortlisted all flying or gliding species. In the second phase, we looked at whether the structures of these species could be applied to human use. It was at this phase that the flying snake was removed from the list of species to be modelled. The flying snake has to continuously move side to side throughout the flight and it can only glide at high speeds [10], making it unsuitable to be adapted to personal flying vehicles. Lastly, in the third stage, similar species were grouped and one in each group was selected to represent the group. This step was to ensure that there were no repeats in structures and thus we could broaden the range of structures to study. It was at this phase that the flying squirrel was removed from the list as it shared a very similar structure with the Malaya Colugo.

The ten species chosen for study are Atlantic Flying fish (Cheilopogon melanurus), Spotted Eagle Ray (Aetobatus narinari), Albatross (Diomedeidae), Malaya Colugo (Galeopterus variegatus), Golden-capped Fruit Bat (Acerodon jubatus), Flying Dragon (Draco Volans), Javan Cucumber (Alsomitra macrocarpa), Sugarcane looper (Mocis frugalis), Kampong (Oroxylum indicum) and Pyralid Moth (Sufetula diminutalis) (Fig. 3).

D. Scale Modelling and Realisation of Distorted Models

Due to the inability of XFLR5 to conduct full-scale analysis, we had to scale our models so as to comply with the software limitations. The official guidelines for XFLR5 suggest that this software cannot handle a full-scale test [11], hence necessitating scaling. In order to keep the consistency with physical wind tunnel testing, we fixed the wingspan at 30cm and let their wing areas vary. This is because the criteria we chose, the CL/CD ratio, is algebraically independent of the wing area. Realistically speaking, we also considered their wing areas, which are determined by the species' body shapes, as a feature of those species to be modelled. As a result of these two reasons, we decided to scale the models to a constant wingspan of 30cm, rather than to a uniform planform area.

Additionally, according to Similitude requirements, the dimensionless quantities, e.g. Reynold numbers should remain the same before and after scaling [12]. However, this will lead to a huge wind speed for scale models when we set the application velocity as 20ms^{-1}, approximately 667 ms^{-1}, or 1.962 Mach equivalent (taking the Javan Cucumber as the example). According to Scaling laws:

$$Re = \left(\frac{\rho V L}{\mu}\right) \quad \rightarrow V_{Model} = V_{application} \times \left(\frac{\rho_a}{\rho_m}\right) \times \left(\frac{MAC_a}{MAC_m}\right) \times \left(\frac{\mu_m}{\mu_a}\right) \qquad \text{--- (3)}$$

$$V_{model} = 20 \times \frac{2.903}{0.08705} = 667\ ms^{-1} = 1.962\ Mach$$

Thus, as we cannot have the models satisfy first-order similarities, we chose to realise distorted models rather than adequate models under the working conditions of full-scale ones. We would then conduct a horizontal analysis across scale models, selecting the best one to conduct the full-scale test in a more advanced and sophisticated software – ANSYS Fluent. The full-scale simulation will suggest the real performance, while scale models are only used in horizontal analysis, i.e. select the ones with better performance among species.

E. 3D Modelling and Analysis Using XFLR5

XFLR5 is an interactive program for the design and analysis of subsonic isolated airfoils, wings or planes designed by a team led by the Massachusetts Institute of Technology(MIT) Professor Mark Drela. In this research, it was used to conduct a preliminary round of analysis on the aerodynamic characteristics of our models. It has been chosen because of two reasons: firstly, it has a user-friendly interface which enable us to conduct XFOIL and 3D analysis on our models in a relatively easy way; moreover, XFLR5 was specially designed for model sailplane designers, therefore it is suitable for the analysis of our wing models which are exactly sailplane wings. Hence, XFLR5 is a feasible and effective software for us to predict the properties of our models.

1) Introduction to the XFOIL and VLM method

The XFLR5 analysis involves two stages: the first is to use XFOIL Direct Analysis to find out the 2D characteristics of a 2D airfoil, and the second is to use 3D analysis to further determine the 3D characteristics of our 3D models to give more accurate predictions on the performance of our models in the real world.

In XFOIL Direct Analysis, given the coordinates specifying the shape of a 2D airfoil, Reynolds and Mach numbers, XFOIL calculated the pressure distribution on the airfoil (both top and bottom surfaces), and hence lift and drag characteristics in different AoAs.

After this, 3D analysis was then carried out. Three methods of 3D analysis are available in XFLR5, which are LLT, VLM and 3D Panel. All of them interpolate the performance of our 3D models (Lift, Drag, Cl and CD etc.) based on the XFOIL Direct Analysis. However, these three methods differ in their way of interpolating, and each of them appeals to different types of wings. In our case, VLM was preferred because of it is the most suitable method to analyse our type of wing. A detailed explanation of VLM and its comparison with other methods will be presented in the following paragraphs.

By summing up vortices all over the wing's planform. VLM can model the perturbation produced by the wing. For every vortex, its strength is calculated out so as to fulfil the appropriate boundary conditions (BC), like non-penetration conditions on the surface of the panels. One thing to take note is that it is the classic VLM being used in our simulation, for which a horseshoe vortex is positioned at the panel quarter chord and the non-penetration condition is set at the three-quarter point.

In VLM analysis, mesh is firstly conducted on the mean camber line of the wing to divide the wing into a number of panels distributed over the span and the chord of the planform, and a vortex (or a doublet and source) is associated to each panel. For wake panels meshed, the wake is simplified as trailing legs of the horseshoe vortices.

The next step after meshing is the calculation. In VLM, lift force and lift coefficient will be firstly calculated out in the following way:

The force on each panel can be calculated using the vector cross product

$$F = \rho V \times \Gamma \qquad \text{--- (2)}$$

Γ is the vortex strength times its length

ρ is the density of the fluid

V is the speed of freestream which implies that the force is normal to each panel.

The lift coefficient is defined as

$$C_L = \frac{1}{\rho S V^2} \sum_{panels} F_{wz} \qquad \text{--- (3)}$$

S being the sum of the panels' area, like the planform area

Fwz is the projection of the force on the vertical axis of wind

This formula can be applied to both chordwise strip and the wing's total surface. As lift force and lift coefficient have been obtained, all the other variables like the pitching moments, centre of pressure position at each span location (which are obtained by summing up the lift force over the panels) and the viscous variables like viscous Cd, transitions, etc can also be interpolated from the value of Cl on the previously XFOIL-generated polars.

2) VLM Comparison with LLT and 3D Panels

VLM is the most suitable method among the three methods XFLR5 provides because it can be applied to any usual wing with low aspect ratio, sweep or high dihedral, including winglets. Since our wing types all have sweep and low aspect, VLM works the best. Other two methods, LLT and 3D panels, both have significant drawbacks that threaten the reliability of our simulations.

LLT method does not mesh the model but use lifting line theory which is a different approach. the limitations of lifting line theory itself may undermine the calculations of LLT method: for non-linear LLT method, its calculation is not a robust process and uses need to choose a relaxation factor carefully. Therefore, LLT is harder to use and may not give accurate results for wings of low aspect ratio and large amounts of sweep.

3D panels, at the other hand, is similar to VLM as it also involves the use of meshing. However, it took into account the thickness of the wings instead of the mean camber line in the case of VLM. There are concrete evidences showing that 3D panels are no better than VLM: in a NASA report [13] the authors firstly used 3D panel, modelling the circulation on the wings with uniform strength doublets, and placing the BC (Neumann type) at the centre of gravity. VLM method was also used, in which a vortex was placed at the panel's 1/4 chord, and the BC point at the panel's 3/4 chord. Both methods have been tested, and the second alternative, VLM, was shown to be better than 3D panel in terms of precision and reliability. Hence the 3D-panel method is not used because of the risk of less precision and reliability.

3) Pre-Validation with NACA 0015

Prior to the simulations, we have to ensure that the data generated by the XFLR5 were valid. We first simulated the airfoil NACA 0015 and compared the simulation results with existing literature and data from previous experiments of the airfoil [14]. In Fig.4, we can observe the results matched in all aerodynamics characteristics, proving the validity of XFLR5 algorithms.

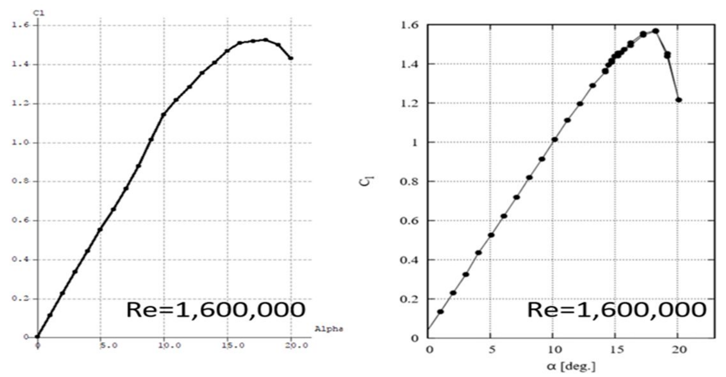

Figure 4. Comparison of simulated and wind tunnel results of NACA 0015

4) *3D-Modeling Using Autodesk CAD and XFLR5*

We searched suitable pictures of the ten species online. Using these pictures, we then plotted the outline of all these models in Autodesk CAD. Instead of uniformly sampling the outlines of selected species, an alternative method of sampling the characteristic points was chosen to sketch the planforms. This is because uniform sampling may require more control points to accurately capture the characteristics of these relatively simple geometries than sampling the points where the curvature of geometry changes rapidly. In practice, the outline was separated into several parts. The coordinates of the turning points and corresponding chord lengths were obtained and then imported into XFLR5. All models used MH 60 airfoil, exported from Profili 2.21, since this airfoil has a high Cl/Cd over a wide range of AoA. This airfoil is also self-stabilizing as it has an "S" shape thickness distribution. This characteristic is helpful in levelling a blended body-wing design aircraft by significantly reducing its pitching moment.

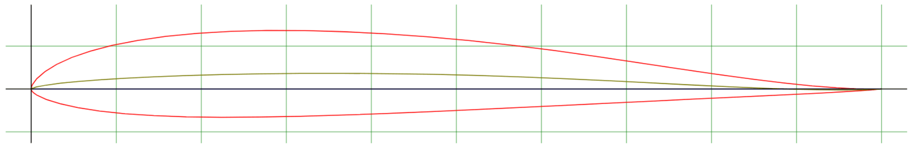

Figure 5. MH 60 airfoil exported from Profili V2.21

Thus, this airfoil was widely used in fly wing designs. Considering the Re number of physical powered gliders, it will perform better than most airfoils when the wingspan is relatively larger [15]. (All models refer to Fig. 6)

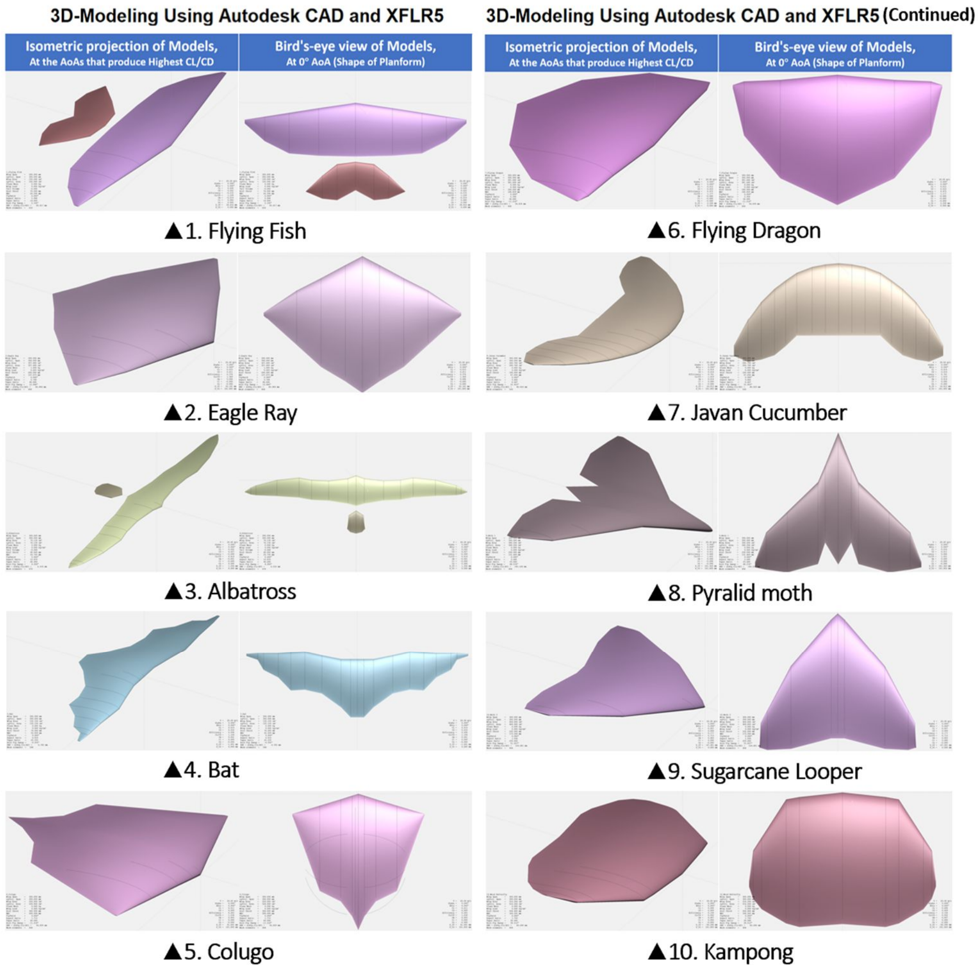

Figure 6. Isometric projection and bird's-eye view of ten models.

5) *Analysis of 10 Models Using XFLR5*

Firstly, we ran the XFOIL Direct Analysis and collected polar data of MH 60 under different Re numbers. The polar curves were obtained through Multi-threaded Batch Analysis from Re 0 to 1,000,000 under Mach 0.059 (20ms-1). The increment for Re was 1000, and the testing AoA was from -20° to 20° with increment of 0.5°. However, in the later tests, the actual models may require a higher pre-calculated Cl of the airfoils due to high AoAs, interfered flows and turbulence, which increase the real Re number of the flow. This was alerted by an error message, e.g. "Span pos = -0.14 m, Re = 48667, Cl = 1.16 could not be interpolated" in the case of Javan Cucumber. To address this problem, we identified the higher Cl value needed in the error display and ran XFOIL Direct Analysis using "fixed Cl" type. Thus, the higher Cl data needed can be directly generated without estimating the AoA or Re number of the air flow in the "fixed speed" type. The speed of 20ms-1 is comparable with the average speed of a Mass Rapid Transit (MRT) train [6] and a current personal flying vehicle, EHANG 184. As its speed is higher, less time is taken to transport commuters, thus fewer vehicles would be using the roads, resulting in less congestions.

We then tested the models with a fixed speed of 20ms^{-1} by using the Horseshoe Vortex (VLM1) analysis method. The analysis sequence started at -2.0° and ended at 15.0° with an increment of 0.5°. The air data was extracted from the U.S. Standard Atmosphere 1976 [17]. The air density is 1.29 kg m^{-3} in the set of data we selected at a temperature of 15°C and altitude of 25m, which is closest to its application environment. All polars are exported and then analysed in Microsoft Excel. The values of their CL divided by their CD gave their CL/CD values (refer to Eqn. 1&2). The higher the ratio, the greater the capability of the models to generate lift and reduce drag. This feature, together with relatively high lift force, indicates the better aerodynamic performance of such a design. The various sets of CL/CD data were then plotted on a graph against the respective AoA.

F. *Verification of Results Using ANSYS Fluent*

1) *Rationale for Selecting Fluent to Verify the Selection of Best Models*

Although the VLM method in XFLR5 has enabled us to do a preliminary comparison of the flying capabilities of 10 species, it has many limitations, like the underestimation of the drag, which will be explained in Chapter IV.A with more details. Due to these limitations which make the XFLR5 results less convincing, a better theory or mathematical model, which takes the viscosity of air into account, should be applied in analysis. The selection based on the results of the improved analysis will verify the previous selection based on XFLR5 results if their indications of the best performing species are identical. In this project, the Navier-Stokes (N-S) equations, available in ANSYS 18.0, were chosen to further model the fluid flow over our models.

Moving a step forward from Euler's Equations, the N-S Equations better described the motion of fluid. This is because the equations not only considered the pressure term due to the Newton's Third Law but also the diffusing viscous term which is proportional to the gradient of velocity. The viscous flow can thus be mathematically modelled and solved, which can compensate the effects of inviscid assumption of fluids in XFLR5's VLM method.

The N-S equations include a time-dependent continuity equation for conservation of mass (eqn.6), a time-dependent conservation of energy equation (eqn.7) and three time-dependent conservation of momentum equations (eqn.8-10). There are 10 variables present in the equations, 4 of them are independent variables and 6 are dependent variables. The 4 independent variables are the x, y, and z as spatial coordinates for the domain and the time t. The 6 dependent variables are the density ρ, pressure p, temperature T (presented by the total energy E_t in the energy equation) and 3 vector components of the velocity: component u in x direction, v in y direction, and w in z direction. The dependent variables are functions of independent variables. The equations are listed below:

Continuity:

$$\frac{\partial \rho}{\partial t}+\frac{\partial(\rho u)}{\partial x}+\frac{\partial(\rho v)}{\partial y}+\frac{\partial(\rho w)}{\partial z}=0 \qquad \text{--- (4)}$$

Energy:

$$\frac{\partial(E_T)}{\partial t}+\frac{\partial(uE_T)}{\partial x}+\frac{\partial(wE_T)}{\partial y}+\frac{\partial(wE_T)}{\partial z}=-\frac{\partial(up)}{\partial x}-\frac{\partial(vp)}{\partial y}-\frac{\partial(wp)}{\partial z}-\frac{1}{Re_r Pr_r}\left(\frac{\partial q_x}{\partial x}+\frac{\partial q_y}{\partial y}+\frac{\partial q}{\partial z}\right)$$
$$+\frac{1}{Re_r}\left[\frac{\partial}{\partial x}\left(u\tau_{xx}+v\tau_{xy}+w\tau_{xz}\right)+\frac{\partial}{\partial y}\left(u\tau_{xy}+v\tau_{yy}+w\tau_{yz}\right)+\frac{\partial}{\partial z}\left(u\tau_{xz}+v\tau_{yz}+w\tau_{zz}\right)\right] \qquad \text{--- (5)}$$

X-Momentum:

$$\frac{\partial(\rho v)}{\partial t}+\frac{\partial(\rho uv)}{\partial x}+\frac{\partial(\rho v^2)}{\partial y}+\frac{\partial(\rho vw)}{\partial z}=-\frac{\partial \rho}{\partial y}+\frac{1}{Re_r}\left[\frac{\partial \tau_{xy}}{\partial x}+\frac{\partial \tau_{yy}}{\partial y}+\frac{\partial \tau_{yz}}{\partial z}\right] \qquad \text{--- (6)}$$

Y-Momentum:

$$\frac{\partial(\rho u)}{\partial t}+\frac{\partial(\rho u^2)}{\partial x}+\frac{\partial(\rho uv)}{\partial y}+\frac{\partial(\rho uw)}{\partial z}=-\frac{\partial \rho}{\partial x}+\frac{1}{Re_r}\left[\frac{\partial \tau_{xx}}{\partial x}+\frac{\partial \tau_{xy}}{\partial y}+\frac{\partial \tau_{xz}}{\partial z}\right] \qquad \text{--- (7)}$$

Z-Momentum:

$$\frac{\partial(\rho w)}{\partial t}+\frac{\partial(\rho uw)}{\partial x}+\frac{\partial(\rho vw)}{\partial y}+\frac{\partial(\rho w^2)}{\partial z}=-\frac{\partial \rho}{\partial z}+\frac{1}{Re_r}\left[\frac{\partial \tau_{xz}}{\partial x}+\frac{\partial \tau_{yz}}{\partial y}+\frac{\partial \tau_{zz}}{\partial z}\right] \qquad \text{--- (8)}$$

Where

$Coordinates:(x,y,z)$	$Time:t$	$Heat\ Flux:q$
	$Density:\rho$	$Reynolds\ Number:\mathrm{Re}$
$Velocity\ Componets:(u,v,w)$	$Total\ Energy:Et$	$Prandtl\ Number:\mathrm{Pr}$

One can easily observe that the N-S equations are mainly partial differential equations that describe fluid flow and energy transfer. However, these partial differential equations are largely unable to be solved analytically. This is because of the difficulty in obtaining the analytical solutions of partial differential equations and especially the closure problem. In the closure problem, the number of equations in N-S equations is smaller than the number of variables, which made the equation unclosed. Hence, approximated numerical solutions using Turbulence Models (TMs) to close the equations may be more practical to obtain. The turbulence modelling and averaging of N-S equations will be introduced later.

Flow domains are then separated into smaller subdomains, which consist of geometric primitives such as tetrahedrals and hexahedrals. The N-S equations are then discretised and numerically solved in these geometrically simple subdomains respectively. For our models, the finite volume method was used to solve the approximate version of the system of equations. Special care was given to ensure a continuity of solutions across the contact regions between two subdomains, which allowed us to integrate approximate solutions inside subdomains to give the overall performance of models in the fluid domain. The subdomains are named as cells or elements, and the assembly of all cells is a mesh. We will later use ICEM-CFD, also an industrial level meshing tool, to manually generate meshes that fit the solver's requirements. The details of meshing process and considerations will be later elaborated in Chapter II.F.5.

However, it is still impractical to solve these equations by hand on hundreds of thousands of elements of the meshes. This difficulty stressed the needs for a powerful computational solver. Therefore, a reputable industrial-grade software, ANSYS Fluent, was chosen as the solver for N-S equations. In our simulations, the air will flow at a low speed of $20ms^{-1}$, in which the air is largely regarded as incompressible. Thus, we follow the convention to choose the pressure-based solver in Fluent, as this solver is designed for low-speed incompressible flows.

In the pressure-based algorithm, the pressure equation is derived from the continuity and the 3 momentum equations, as stated in the ANSYS official guidelines. The Fluent thus solves the pressure equation to achieve the continuity of the velocity field. Because the pressure equations are also nonlinear and start with a guess of the pressure, the solving process involves iterations until the solution converges.

Based on the expected accuracy of results, we selected the pressure-based coupled solver. According to the ANSYS official documents, its coupled algorithm solves a coupled system of the momentum equations and the pressure-based continuity equation. As the equations are solved together, the speed of convergence significantly increases compared to other algorithms. For steady-state flows, the implementation of the coupled algorithm is also more robust. Instead of the conventional SIMPLE or SIMPLEC methods implemented in the pressure-based segregated algorithm or density-based algorithm, pressure-based coupled algorithm provides a more accurate alternative. The coupling is achieved through an implicit discretization of the pressure gradient terms in the momentum equations, and an implicit discretization of the face mass flux.

In the discretised momentum equation:

$$a_p u = \sum_{nb} a_{nb} u_{nb} + \sum p_f A \cdot i + S \qquad \text{--- (9)}$$

the pressure gradient for component K is:

$$\sum_f p_f A_k = -\sum_j a^{u_k p} p_j \qquad \text{--- (10)}$$

Here $a^{u}{}_{k}{}^{p}$ is the coefficient derived from the Gauss divergence theorem.

The P_f is calculated in the form of

$$P_f = \frac{\frac{P_{c_0}}{a_{pc_0}} + \frac{P_{c_1}}{a_{pc1}}}{\frac{1}{a_{pc_0}} + \frac{1}{a_{pc1}}} \quad \text{--- (11)}$$

:

Then, for an arbitrary i^{th} cell, the discretised momentum equation for component K is:

$$\sum_j a_{ij}{}^{u_k u_k} u_{kj} + \sum_j a_{ij}{}^{u_k p} p_j = b_i^{u_k} \quad \text{--- (12)}$$

For the discretised continuity equation:

$$\sum_f^{N_{faces}} J_f A_f = 0 \quad \text{--- (13)}$$

The algorithm replaces the balance of fluxes by the flux expression:

$$Jf = \rho_f \frac{a_{pc_0} v_{nc_0} + a_{pc_1} v_{nc_1}}{a_{pc_0} + a_{pc_1}} + d_f \left(\left(p_{c_0} + (\nabla p)_{c_0} \cdot \vec{r}_0 \right) - \left(p_{c_1} + (\nabla p)_{c1} \cdot \vec{r}_1 \right) \right) = \hat{J}_f + d_f \left(p_{c_0} - p_{c_1} \right)$$

--- (14)

which gives the form of discretisation:

$$\sum_k \sum_j a_{ij}{}^{pu_k} u_{kj} + \sum_j a_{ij}{}^{pp} p_j = b_i^p \quad \text{--- (15)}$$

Hence, we obtained the overall system of equations

$$\sum_j a_{ij}{}^{u_k u_k} u_{kj} + \sum_j a_{ij}{}^{u_k p} p_j = b_i^{u_k} \quad \text{and} \quad \sum_k \sum_j a_{ij}{}^{pu_k} u_{kj} + \sum_j a_{ij}{}^{pp} p_j = b_i^p$$

Transform these two equations into the δ-form, the overall system of equations become:

$$\sum_j [A]_{ij} \vec{X}_j = \vec{B}_i \quad \text{--- (16)}$$

In which the influence of an element i on an element j is described by the matrix:

$$A_{ij} = \begin{bmatrix} a_{ij}^{pp} & a_{ij}^{pu} & a_{ij}^{pv} & a_{ij}^{pw} \\ a_{ij}^{up} & a_{ij}^{uu} & a_{ij}^{uv} & a_{ij}^{uw} \\ a_{ij}^{vp} & a_{ij}^{vu} & a_{ij}^{vv} & a_{ij}^{vw} \\ a_{ij}^{wp} & a_{ij}^{wu} & a_{ij}^{wv} & a_{ij}^{ww} \end{bmatrix} \quad \text{--- (17)}$$

and the unknown and residual vectors also comes in matrices:

$$\overrightarrow{X_j} = \begin{bmatrix} p_i' \\ u_i' \\ v_i' \\ w_i' \end{bmatrix} \quad \text{--- (14)} \qquad \overrightarrow{B_i} = \begin{bmatrix} -r_i^p \\ -r_i^p \\ -r_i^p{}_i \\ -r_i^p \end{bmatrix} \quad \text{--- (18)}$$

Here it is observed that the influence Equation of an element *i* on an element *j* (Eqn.19), together with its unknown and residual vectors, are in the form of the coupled Algebraic MultiGrid (AMG). We can then deploy the Coupled AMG Solvers in ANSYS to find the numerical values of them.

At this point, the numerical solutions of discretised N-S Equations were obtained and the residuals of the solutions were calculated. The accuracy of the solutions was also obtained, as a smaller residual indicates a higher accuracy. This residual has a great significance as it indicates the discrepancy between numerical values and ideal analytical solutions of the N-S equations. In meshing and calculations, the residual will be reduced by improve the meshing quality and increase the number of iterations, which will be mentioned in Chapter II.F.5.

2) *Turbulence Modelling*

Another governing model in simulating the actual fluid flow is the turbulence modelling. The N-S equations describe the pressure and velocity of the fluid flow, and these 2 quantities are decomposed into a mean part and a fluctuating part. To model the mean flow, the N-S Equations are averaged to give the Reynolds-Averaged Navier-Stokes (RANS) equations. Because of the non-linearity of the N-S equation, the fluctuating part of velocity still exist in the RANS equations. One term contributes to the non-linearity is the Reynold stress: $-\rho\overline{v_i'v_j'}$. With this term, the number of equations is smaller than the number of unknowns. Thus, the Turbulence Models (TM) are used to empirically assume these values. Additionally, TMs are also useful as they help to model the non-linear term, $\frac{\partial}{\partial x_i}(\overline{\rho u'_i u'_j})$, of the momentum transportation equation of N-S equations:

$$\frac{\partial(\rho u_i)}{\partial t} + \frac{\partial(\rho u_i u_j)}{\partial x_i} = -\frac{\partial p}{\partial x_j} + \frac{\partial}{\partial x_j}(\mu \frac{\partial u_i}{\partial u_j}) - \frac{\partial}{\partial x_j}(\overline{\rho u'_i u'_j}) + F_i \quad \text{--- (19)}$$

Considering the low Re number of the air flow and the limited computing power we have, we selected the Spalart–Allmaras turbulence model (S-A model) to be used in Fluent calculations.

The S-A model is a one-equation model which solves a transport equation for the kinematic eddy turbulent viscosity [23]. The S-A model was devised specifically for aeronautic uses, which produced fair results for boundary layers which are subjected to adverse pressure gradients. The original model was an accurate low Re number model, which needed the first layer height of mesh elements in viscous sublayer and buffer layer to be small enough. The transport equation is given as:

$$\partial/\partial t(\rho \tilde{v}) + \frac{\partial}{\partial x_i}(\rho\tilde{v}u_i) = G_v + \frac{1}{\sigma_{\tilde{v}}}\left\{\partial/(\partial x\_j)\left[(\mu + \rho\tilde{v})\frac{\partial \tilde{v}}{\partial x_j}\right] + C_{b2}\rho\left(\frac{\partial \tilde{v}}{\partial x_j}\right)^2\right\} - Y_v + S_{\tilde{v}}$$

--- (20)

To close this equation, three following equations were introduced:

$$\nu_t = \tilde{\nu} f_{v1} : Kinematic\ eddy\ viscosity \qquad \text{--- (21)}$$

$$f_{v1} = \frac{\chi^3}{\chi^3 + C_{v1}^3} : Viscous\ damping\ function \qquad \text{--- (22)}$$

$$\chi = \frac{\tilde{\nu}}{\nu} : Kinematic\ viscosity\ ratio \qquad \text{--- (23)}$$

To describe the wall distance, the dimensionless y+ value is introduced as:

$$y^+ = \frac{y u_\tau}{\nu} \qquad \text{--- (24)}$$

$$u_\tau = \sqrt{\frac{\tau_{wall}}{\rho}} \qquad \text{--- (25)}$$

where u_τ is the friction velocity at the nearest wall, y is the distance to the nearest wall and ν is the local kinematic viscosity of the air. A more refined volumetric mesh in the boundary layer will results in a lower y+ value. If the y+ value is smaller than one, the mesh is considered fine enough to perform calculation in the viscous sublayer and buffer layer, which fully takes the viscosity of fluid at low Re number in near boundary layer into account. Thus, our meshes which had $y+ < 1$ were qualified to adopt TMs which modelled the influence of the Reynolds stress tensor mentioned in Chapter II.F.2. In addition, the S-A model was a one-equation TM, which will reduce the computing power needed in later calculations. As we only had personal laptops to perform simulations, the reduction in TM's complexity could contribute less to the time constraints. Therefore, the S-A model in Fluent became the most suitable TM to apply in our simulations.

3) Re-Modelling Using CATIA

As mentioned in Chapter II.E.4, we have 3D modelled the geometries of all species in XFLR5. However, the 3D geometries in XFLR5 can only be exported in .stl format, which storage approximated faces in triangles rather than fine surfaces. This made the geometries unsuitable to be processed in ICEM-CFD and Fluent, as the surfaces are too rough and contain too much triangular elements. Therefore, another industrial level 3D modelling software, CATIA, was chosen to re-model all species. Considering the ease of use and the productivity, the Generative Design module, which provides plenty of powerful functions, was chosen as the working environment. The same sets of control points were used to sketch the planforms on the XY plane and the same airfoil, the MH 60, was sketched in the XZ plane using spline curves. The 3D geometries were created by the Swept Volume function provided by the Generative Design Module, which were essentially solid bodies created when the airfoil sweeps and resizes along the leading edge and trailing edge of the planform in Fig.7&8. These solid bodies thus had the same geometries as the models in the XFLR5.

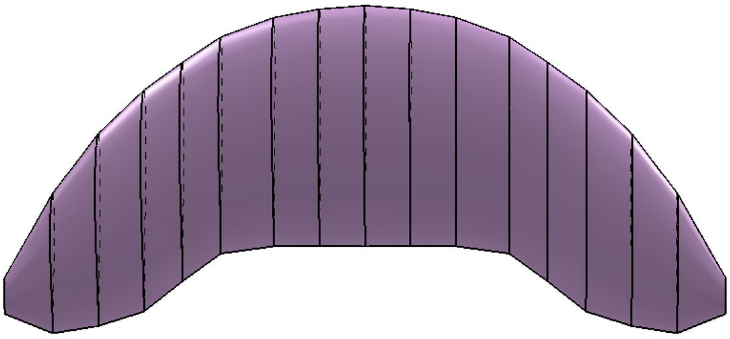

Figure 7. The Bird Eye's View of One CATIA Model.

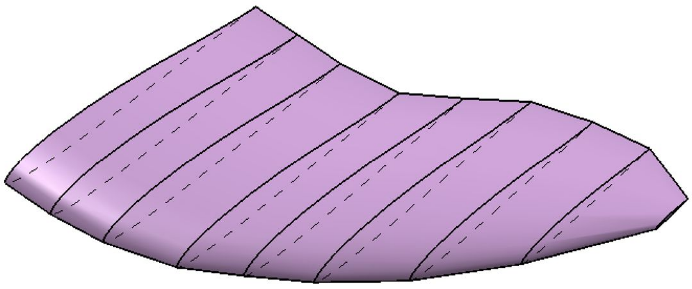

Figure 8. The Isometric Projection of a Half-Model Which Was Later Used in Meshing.

4) *Importing CATIA Geometries and Creating Large Size Flow Domain*

After we modelled all species with CATIA, the 3D files were exported into .stp format, which is readable and editable in all software involving 3D geometry. Those .stp files were then imported in the SpaceClaim provided by ANSYS, in which an enclosure was generated as the flow domain to be used later. To fully simulate a free-stream flow with all details of the flow before, over and after the model, a large-size enclosure was created. Following the empirical knowledges, the distances of the walls before and after the model are greater than 20 times of model's Mean Aerodynamic Chord (MAC), and the distances of the walls above, below, and from the wing tips are greater than 16 times of the model's MAC. The rationale for choosing such a large flow domain is to minimise the influences of wall effect and other factors. The accuracy of the simulation can thus be improved.

5) *Meshing with ICEM-CFD*

The SpaceClaim files, which consist of CATIA-generated geometries of species and the large-size flow domain, were imported into ICEM-CFD to be manually meshed for better mesh quality.

The models were imported into ICEM-CFD and half-models were used for the meshing since all tested models featured symmetric aerodynamic characteristics. The aerodynamic characteristics of the whole models can be obtained by simply doubled the data generated from half-model simulation, as the flow patterns are symmetrical. Moreover, this planar symmetry will speed up the calculation for CFD by at least 50% or more in simulation turnaround time, especially efficient when there are hundreds of cases to be simulated for this project. The meshes adopted CH-Grid topology, which mainly consists of Hexa elements. This topology was widely used in aircraft meshing, as it ensures accuracy and efficiency in the meantime.

The flow domain, also called enclosure in SpaceClaim, had a shape illustrated in Fig. 9. The enclosure consists of two parts, a semi-cylindrical and a square prism. The foremost ends of the models were set as the origin and a semicircle of the enclosure with radius of 20 times of the corresponding model's MAC is created. The flow domain of trailing edge was also generated with a length of 20 times of MAC and a width of 16 times of MAC, illustrated in Fig. 10. This large flow domain will minimise the influences of wall effect and other factors to improve the accuracy of the simulation. Most models were separated into three parts: ROOT, MID, TIP in the meshing with greatest effort to capture the features of the models.

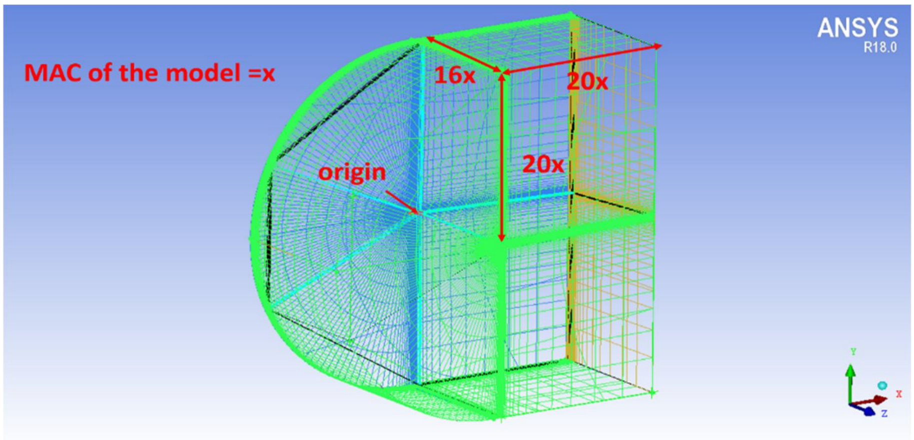

Figure 9. The enclosure of half-models after meshed by ICEM-CFD

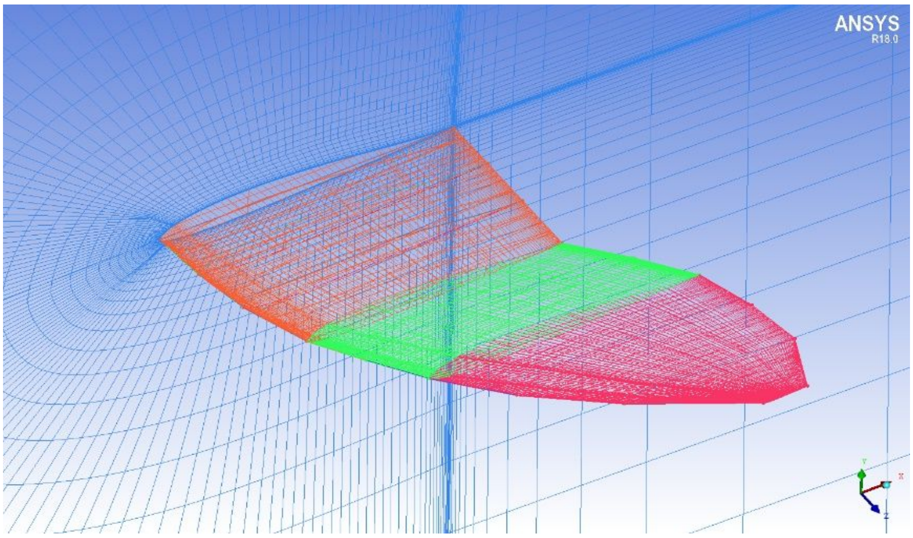

Figure 10. Meshing of Refined Javan Cucumber in ICEM-CFD.

The Boundary Layer was created by blocking technique near the surface of the model with 20 nodes. The spacing 1 was set to be 0 and spacing 2 was 1e-5. The ratio 1 and ratio 2, which were the inflation rates, were both set to be 1.2. These settings greatly reduced the y+ value to around 0.4 for more than 90% of the cells. As mentioned in Chapter II.F.2, this low y+ value enable us to adopt S-A model for turbulence modelling under low Re number. The leading edge was set with 30 nodes and the tip was set with 20 nodes since air particles near these regions change their motion most fiercely. With more and finer nodes for these regions, the motion of the air particles can be better simulated. Conventional setting was applied for other parts. The mesh was then refined until the negative volume elements was fixed.

Y-Block was utilised to solve the disadvantages of meshing due to the limitations of ICEM for the triangular meshing elements. This will also improve the simulation at the leading edge of the models, where is one of the most critical parts for the simulation. All the cross sections were adjusted to create a smoother meshing surface of the models. The quality of the meshing was refined until the Determinant (2x2x2 stencil) was greater than 0.60.

6) Fluent Set-Ups

Despite the meshes we produced in ICEM-CFD were structured hexahedral meshes, the Fluent solvers can only process unstructured meshes. In this case, the structured meshes in ICEM-CFD were exported to Fluent in Fluent 4 format, which allows Fluent to convert them into unstructured meshes.

After loading the mesh files into the Fluent, other parameters were also set according to our requirements. The Energy Equations and Heat Exchanger were switched off, as the solutions under low-speed incompressible flow in our cases may not require these equations to converge and stay accurate. The Spalart-Allmaras was selected to be the turbulence model, and the reason was introduced in Chapter II.F.2 before. The fluid type was set as "air" with the density of 1.29kg m^{-3} under 288.76K, identical to the conditions we extracted from the database [17] and used in XFLR5. In the "Boundary Conditions" tab, we designated specific walls of the enclosure to be the velocity-inlet and pressure-outlet. The Velocity Magnitude was 20ms^{-1}, and the coordinate system was set to be "Cartesian (X,Y,Z)". This transformation will be further discussed in the data collection, process and analysis in Chapter II.F.8.

The pressure-based coupled solver was chosen to couple the pressure with velocity, and the reason was explained in Chapter II.F.1. The parameters of the solver were chosen according to theoretical knowledge and empirical experiences for a higher accuracy. For spatial discretisation, the pressure, momentum and modified turbulent viscosity were all in second order. All under-relaxation factors, include pressure, density, forces, momentum and turbulent viscosity, were reduced to 0.3. For better convergence and smaller residuals, the Courant Number was set to 0.5. In overall, the parameters were optimised for more accurate results.

7) Fluent Calculations with MATLAB Journal for Auto-AoA Alteration

In practice, the results were deemed accurate if the solution converges and the scaled residuals are smaller than 1e-6. To let the solution converge and reduce the residuals, we performed 200 iterations on the scaled models. Together with the optimised parameters in Fluent, we predicted that the solutions may converge after 100 iterations and the final residuals may be reduced to around 1e-7.

However, the Fluent had no embedded function to automatically change the direction of the incident flow. Traditionally, the X-component and Y-component of the flow were manually input to adjust the AoA. This process was time-consuming and typing error may happen. Thus, we wrote a MATLAB journal to save the case and data after a successful calculation, then input the X and Y component for the next AoA and launch the calculation again. This journal automated the calculation, which compensated the increased time spending on solving the refined meshes in Fluent.

8) Data Collection, Process and Analysis

After the calculation, the data generated will be saved in report files. To read the data from files, Tecplot 360 was used to both visualise the force convergence and residuals and export the lift, drag and their coefficients into Excel sheets. These data, however, were not directly usable. This is because the Fluent results were calculated in Body Coordinates, in which the forces were defined with regards to the orientation of the moving aircraft. However, the standard aerodynamic forces, include lift and drag, are defined in Wind Coordinates which take references to the flow direction. These two coordinate systems are different when AoA is not zero. Thus, we needed to perform a coordinate system transformation, by which the body coordinates data was transformed to wind coordinates data. The equation is illustrated in Fig.11.

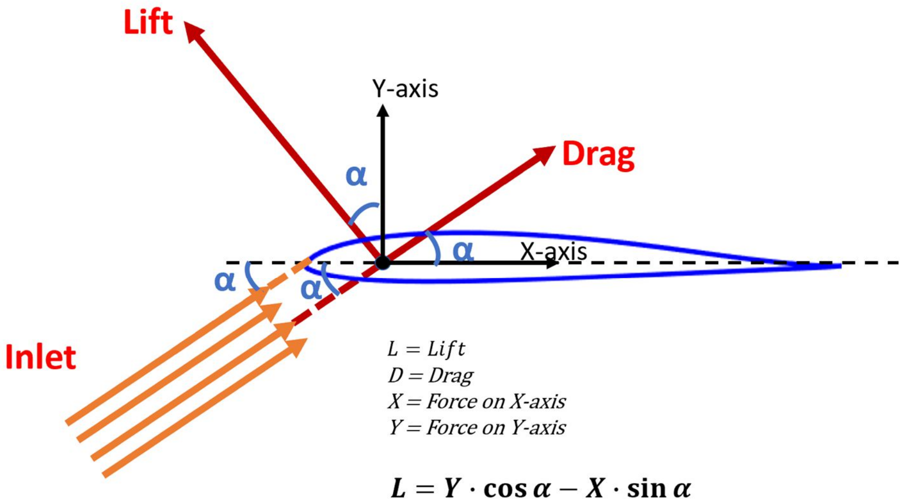

$$\boldsymbol{L = Y \cdot \cos\alpha - X \cdot \sin\alpha}$$

$$\mathbf{D = X \cdot \cos\alpha + Y \cdot \sin\alpha}$$

Figure 11. Graphical illustration of coordinate transformation.

After the coordinate transformations, the CL and CD data from Fluent and XFLR5 were plotted against the AoA in Origin, which is a professional plotting software designed for scientific uses. These graphs will illustrate the discrepancy between XFLR5 results and Fluent data, and similar trends with relatively small discrepancies will suggest that the XFLR5 results were verified. The CL/CD data from Fluent were then plotted against the AoA. This graph will be compared to the CL/CD-AoA graph from XFLR5, which will verify our selection of the best performing species. If the selected species have the highest CL/CD and are able to sustain it in a large range of AoA in both graphs, the selection of the best performing models is verified.

G. Experimental Validation using Wind Tunnel:

The aerospace industries generally hold a suspecting view on the CFD results. Even the CFD data corroborate with each other, their source of computation is eventually a virtual method. Hence, to physically observe the performance of the top performing models, wind tunnel experiments were conducted on the 2 best performing species.

1) Rationale for Selecting the Half-Model Method

In this research, a Gunt HM 170 open loop wind tunnel was used to conduct experiments in order to validate our simulated data. The measuring section of the wind tunnel had a dimension of 29.2*29.2*42cm [18]. The conventional method tests the whole model in the test section. However, to best utilise the limited space, a different testing method, which tests the performance of half-models, was deployed. The distance between the wingtips and the wall should be at least a half of the wing span to reduce the wall effects on the flow patterns. Therefore, the span of the test full-models should only be maximumly 15cm. However, if we apply the half-model method, even the span of the half-model will be maximumly 15cm and thus the wing span of the original model will become 30cm, 2 times larger than the wind span we can achieve in full-model method. A greater wing span will help to reduce the percentage effect of the downwash, which causes the induced drag. Therefore, the overall performances of the scaled models will be more similar to those of full-size ones, making the parallel comparison between species more convincing and accurate.

2) Modification of Models

Three modifications were made to the half-wing models from Fluent analysis. First, we designed a hole to place the supportive rod for the later testing. Ideally, the supportive rod should be placed at the Center of Pressure (CP) of the wing, where the aerodynamic forces are directly applied on. It is impractical, however, to assume a fixed position of CP as it moves significantly with AoA. We overcome this problem by placing the hole for supportive rod at the position of Aerodynamic Center (AC), following the conventions of wind tunnel experiments. The AC is a point at where the pitching moment of an airfoil or wing stays constant, and usually being calculated as the 25% point of the MAC. According to *Model Aircraft Aerodynamics* [8], the distance between AC and CP is usually small enough to be neglected (2%-3% of the base chord) and this makes the positioning of the hole at AC a viable alternative. Therefore, the hole was designed to have a cylindrical shape with a base diameter of 4.3mm. As the rod has a diameter of 4mm, the 0.3mm tolerance allowed the rod to be glued securely in place for later tests.

The second modification is the addition of brims on the surfaces where the models were split into half. These brims acted as end plates in later tests to stop the pressure difference between the top and bottom of the wing to create a downwash at the surface. By doing so, the half wings can perform more similar to the full wing in terms of flow patterns. Moreover, as the thickness of the end plates was 0.3mm, its own aerodynamic forces can be considered negligible. More accurate and convincing results of the wind tunnel test can thus be expected. For the ease of modelling and printing, the end plate was glued to the model after printing and polishing.

The third modification specifically came to the model of Javan Cucumber. Its swept wing moved the position of AC more backward than non-swept wings. However, the thickness of the model at the point was too small to firmly hold the rod in place under a strong wind of $20ms^{-1}$. This weakness suggested the need for structural reinforcement of the supportive hole. We thus deployed a slight inflation of the geometry around the hole, by which the wall thickness was increased to 1 mm. Fig.12. However, this modification may slightly affect the result of Javan Cucumber. Despite this, as the slight inflation was relatively negligible compared to the whole geometry of the model, we predicted that its effects on the results would not be significant enough to warrant considerations.

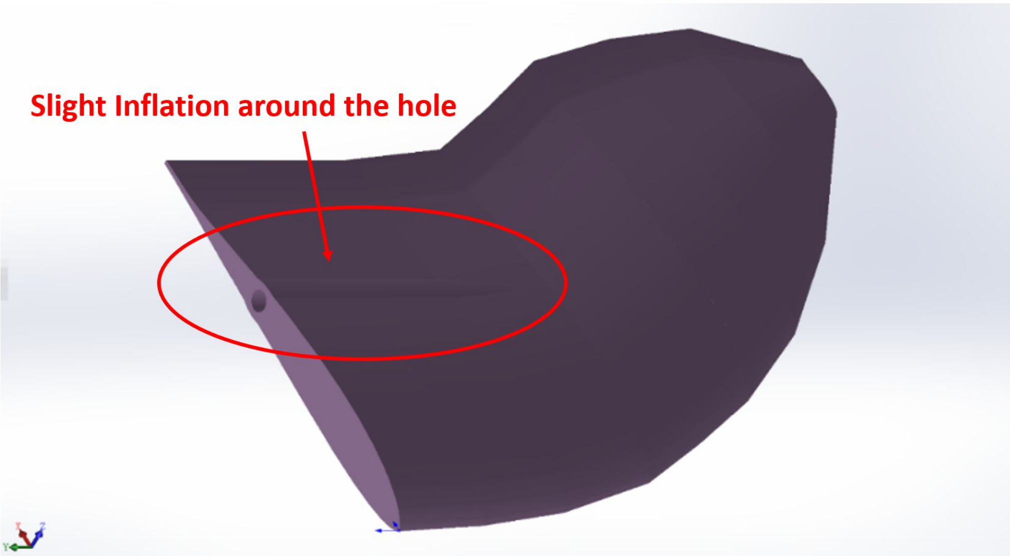

Figure 12. The Modified Model of Javan Cucumber

3) Manufacture the Wind Tunnel Models through 3D Printing

Considering the time convenience and cost constraints, Fused Deposition Modelling (FDM) 3D printing was chosen to manufacture our wind tunnel test models. This method was the most widely used one and was the fastest among all 3D printing techniques, which could save the time for a more extensive project. This method also uses low-cost Polylactic Acid (PLA) plastic. The PLA plastic has a relatively low hardness, which also made the sanding and polishing easier.

The 3D printer we purchased was 4MAX from Anycubic Co. Ltd, which was designed for semi-industrial or high-performance desktop use.(Fig. 13) The resolution on the X and Y axis is 0.0125mm, and 0.0025 in the Z axis. This resolution was considered largely sufficient for our wind tunnel models.

After making the 3 modification of our models, those 3 models were printed with the highest accuracy and resolution. The layer height was set as 0.1mm, which considerably reduced the surface roughness brought by the laminated structure from layer-by-layer additive manufacturing [19]. Later, the models were well-sanded by sand papers until 2000 grits and polished with Tamiya polishing compounds until the "finish" level. This sanding and polishing process totally removed the laminated structure and its roughness, which created mirror-like surfaces of the models. Thus, the drag due to surface roughness will be minimised to keep the results accurate.

After the polishing process, a cylindrical stainless-steel rod was glued in the hole of each model. This rod will later serve as the connection between the model and the force sensor. For a more accurate result, we chose stainless steel as the material as it is not only stronger than copper or aluminium but also readily available in hardware shops. The diameter of the rods can thus be reduced to 4 mm, which would produce less interference in the wind tunnel.

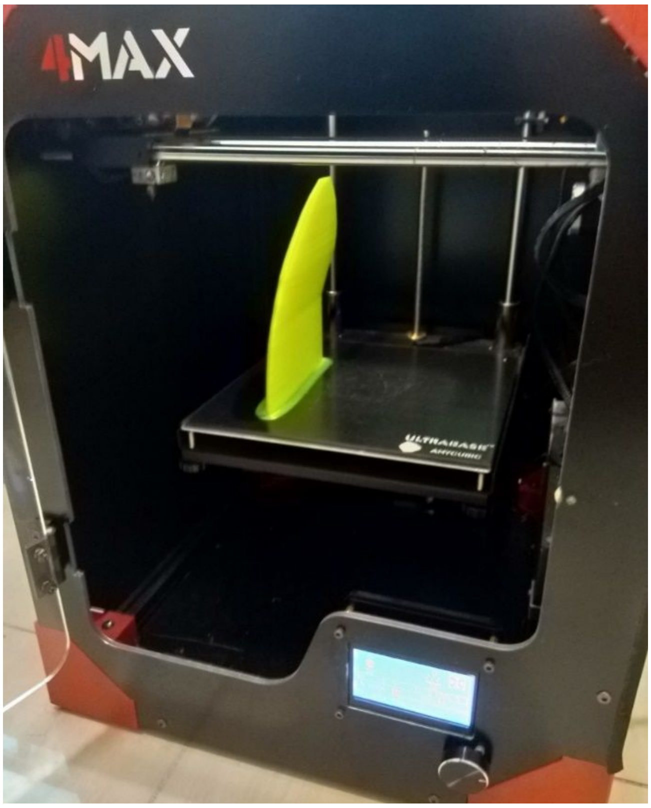

Figure 13. 3D Printing of the Models Using PLA Plastic

Figure 14. Three Models Printed for Pre-Validation and Validations

4) *Experimental Set-ups*

As aforementioned, a Gunt HM 170 educational open return wind tunnel was chosen to conduct the experiments. (refer to Fig. 15)The details of the wind tunnel are illustrated in Fig.15. After split the models into half, the left-hand-side parts, the same side as in the Fluent, was originally chosen to be tested. The model was placed vertically with the wingtips pointing upwards. The lift will then be sideward and the drag backward. The two-component force sensor was placed under the model, and the orientation of the sensor was adjusted that the direction of positive drag was parallel to the flow direction, and the direction of positive lift was perpendicular to the flow direction. This is illustrated in Fig.16.

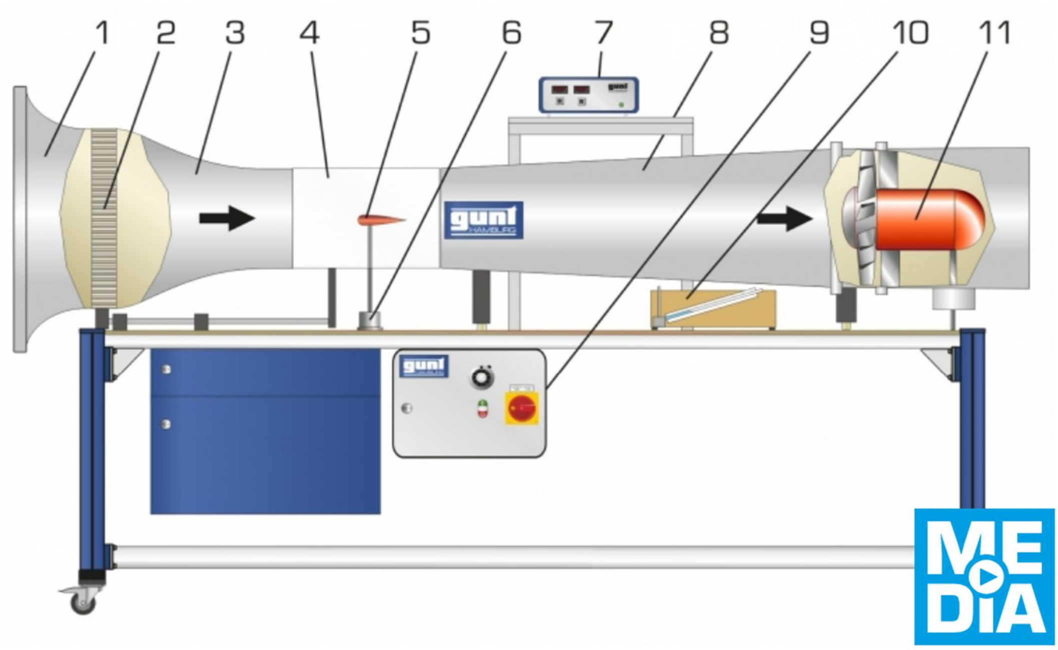

1 inlet contour, 2 flow straightener, 3 nozzle, 4 measuring section, 5 model, 6 force sensor, 7 display and control unit, 8 diffuser, 9 switch cabinet, 10 inclined tube manometer, 11 axial fan

Figure 15. Components of the educational wind tunnel

Figure 16. Installation of Models in the Test Section and Placement of the Force Sensor

Above the force sensor was a rotational plate, on which has the degree markings around its circumference. Later, we will rotate this plate to adjust the angle between the model and the direction of flow. Thus, the rotation was essentially a manipulation to adjust the AoA of models. We will read the AoA of the model from the degree markings on the circumference.

Figure 17. Degree markings and zero graduation indication on the rotational plate

After turned on the wind tunnel, the wind speed was read on the liquid barometer at the right to the data logger. We then read the bottom of the concave meniscus in the barometer. The rotational speed of the suction turbine motor in the wind tunnel was adjusted till the bottom of the meniscus hit the reading of 20ms-1. We then waited for another 5s for the reading to stabilise. If the barometer reading deviated, we made corrections by adjusting the rotational frequency of the motor.

Figure 18. Liquid barometer as an indication of the air speed.

The lift and drag force will be directly read from the digital datalogger. The method to collect these data was further introduced in Chapter II.G.7. However, we encountered a sensor malfunction in the positive direction of lift, as the reading saturated at around 0.47N. Therefore, we decided to use the right-hand-side models whose lift will be in the sensor's negative direction of lift. The two results should be the same except for the symbol, as the flow patterns are symmetrical and the Re number the same across the two sides. We will later multiply the lift readings with -1 to obtain the real lift data.

Figure 19. HM 170 Digital datalogger which displayed the Lift and Drag.

5) Validation with NACA 0012 Standard Wing Section

The wind tunnel, however, may have its systematic errors as an experimental equipment. These errors may come from the two-component force sensor, the turbulence in the airflow and inaccurate readings of the wind speed and AoA. In the pre-validation, the results from our experiments will be compared with existing literatures. By this comparison we can find out the accuracy of our wind tunnel.

However, it was hard to find a piece of corroborated data for NACA 0012 airfoil and other NACA airfoils under low Re numbers. The minimum Re number of the corroborated data was 360000[24], which was far greater than the test condition of our actual experiments. Hence, we used a set of uncorroborated data which investigated on the performance and non-linearity of NACA 0012 at Re 60000-100000[ohtake, 2007]. These data may not be fully accurate but still valuable as they indicated the aerodynamic characteristics of NACA 0012 in the Re number close to our actual experiments and simulations. We would later compare the results from Fluent simulation, existing literature and our wind tunnel test to investigate the discrepancy among these 3 sets of data. This will provide a sense of the accuracy of both wind tunnel testing and CFD simulation.

The aerodynamic characteristics we used for comparison were the CL and the CD. However, the method to eliminate the downwash to simulate a 2D flow in the existing literature, which connected the two ends of the airfoil section to the top and bottom walls of the wind tunnel, was not applicable to our wind tunnel. To address this issue, we installed two end plates at the sides of the airfoil section. The end plates, as aforementioned, will supress the tendency of the flow from high-pressure top surface to the low-pressure bottom surface This will eliminate the effects of the downwash at the wing tips, by which the flow pattern over the section will show resemblance to the 2D flow over the airfoil. This similarity enabled us to compare our wind tunnel result with the existing literature.

6) Actual Testing of Two Best Performing Species

The two best performing species selected previously were then tested in the wind tunnel. The wind speed was 20ms-1. The room was air-conditioned at 16°C so as to best comply with the air data selected in the database used in previous CFD simulations. The altitude of the wind tunnel laboratory is around 25 meters above the sea level, which is also identical to the data's condition.

As mentioned in the Chapter II.G.2, a stainless rod was glued in the designed hole. The rod was then placed in the slot on the force sensor. We would then measure the lift and drag forces of these two models under the AoAs of -2, 0, 2, 5, 8, 10, 12 and 15 (degree). The 8 data points would allow us to plot graphs of any shapes.

7) Data Collection and Analysis

The data output ports of the two force sensors for lift and drag were connect to a data displayer, which has two screens showing the lift and the drag respectively. We recorded the data by taking videos of the screens, since the number displayed may keep changing, especially when the stall occurred. For every experiment, we took a video which was 5 seconds long. Every video was then divided into 25-time frames, every time frame 0.2s long. A total of 25 sets lift and drag data displayed in these 25-time frames were then obtained. The average lift and drag data for every experiment was then calculated out by taking the average of these 25 pairs of data. Lastly, we will calculate out the average of the two sets of the average lift and drag data from the two experiments under the same AoA (as aforementioned, for every AoA, two experiments under the same conditions had been conducted) to get the real average lift and drag under every AoA.

Figure 20. A Screen Shot of the Force Sensor with Readings

H. Analysis of Conventional Design Using ANSYS Fluent

The conventional design of the delta wing was also analysed in ANSYS Fluent. We took the example of XT912 Tundra-Merlin, a popular powered glider that is readily available in the market with excellent aerodynamic performance. The wingspan of the 3D model was 10.0 m and the airfoil applied was also MH 60. We constructed and meshed this model using the same methods in Chapter II.F. However, the analysis on the model was modified. Realising the limitation of S-A model mentioned in Chapter IV.B, a more advanced and widely applied two-equation TM, the k-ε model, was chosen for the simulations of full-scale models. The k-ε TM models both the turbulence kinetic energy k and the rate of dissipation of turbulence energy ε. Compared to the previously used one-equation S-A model, the k-ε model also takes the ε into account, which in turn lead to more accurate results. To deal with the increased time complexity of the k-ε model, a 16-core computing workstation was used in full-scale simulations. This will greatly reduce the time costs and thus increase the overall efficiency.

Figure 21. A commercially available model of XT912 Tundra Merlin

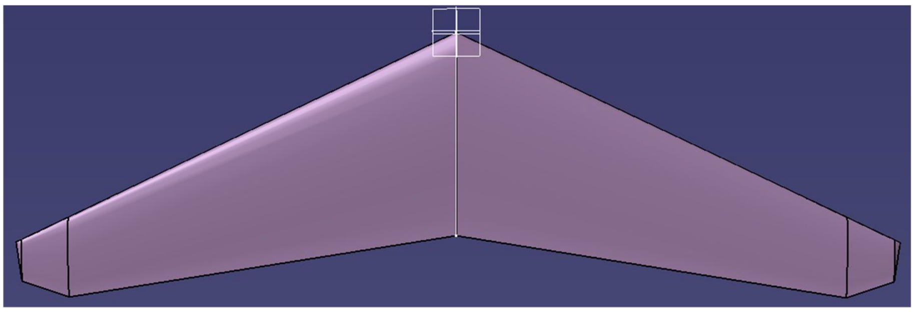

Figure 22. Wing of XT912 Tundra-Merlin in CATIA V5

I. Full-Scale Javan Cucumber Model Simulation Using ANSYS Fluent

Due to the limitations in software algorithm mentioned in Chapter IV.A, XFLR5 is not suitable to simulate full-scale models. Thus, we decided to use ANSYS Fluent for the full-scale simulation. Taking current commercial powered gliders as references, we designed the full-scale model of the best model with a wingspan of 10.0 meters. The 3D model of the best one was further refined by adding new control points in its planform in CATIA. It was also meshed in ICEM-CFD using C-H grid topology (Fig. 9) and later simulated in ANSYS Fluent under the same condition experienced by its scaled counterpart and the conventional design. Lastly, the post-processing was done in Tecplot 360. (Fig. 23).

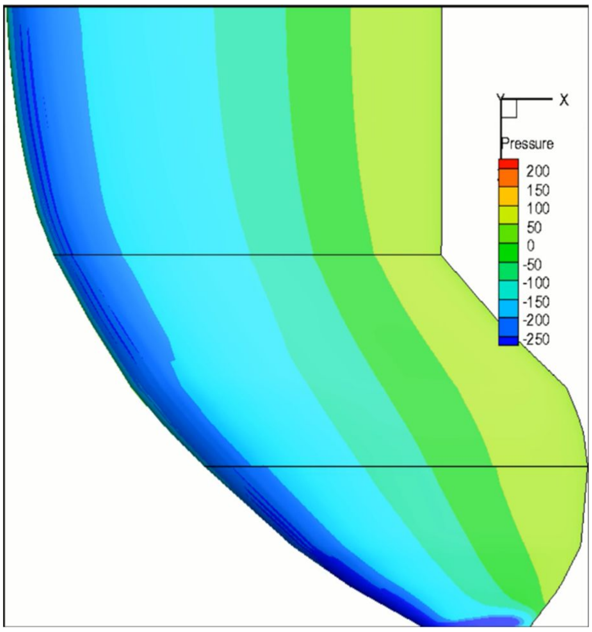

Figure 23. Visualisation of Pressure Distribution of Refined Javan Cucumber in Tecplot.

One point worth noting was the reduced residuals on full-scaled models. Staying unsatisfactory about the residuals of scaled models, we have refined the meshes of the full-scaled models in the ways mentioned in Chapter II.I. After 500 iterations, the residuals for all forces should be reduced to a magnitude below 1e-6. To ensure a better accuracy, we aimed at further reducing it below 1e-9 and ran 2000 iterations per case.

J. Prototyping

After previous testing and experiments, we manufactured a prototype of the best model with a wingspan of 50cm. We select this wingspan according to the machine's limits. We used Computer Numerical Control (CNC) to mill the model out from a block of Expanded Polypropylene (EPP). The software called Mach3 was used to generate the G-codes which controlled the CNC machine from the model's 3D geometry. Later, the CNC machine will read these codes and mill out surfaces on a block of EPP foam. By doing this for the upper and bottom surfaces of the wing, our prototype can be manufactured.

This prototype was installed on a MAV (refer to Fig.26) as the test platform to examine the flying capability of such a design. The MAV was manufactured through laser cutting of KT foam board (refer to Fig. 24&25). The model of laser cutter we used was REDSAIL CM-1690.

The model will be launched from ground and we will monitor its take-off speed. We will also find out the minimum throttle for the new model to maintain level flight at a constant AoA. The hovering will also be performed to check its loss in speed when turning. We will then compare these three tests with the previous flight with a conventional wing. These three indicators will then qualitatively depict the performance of our prototype.

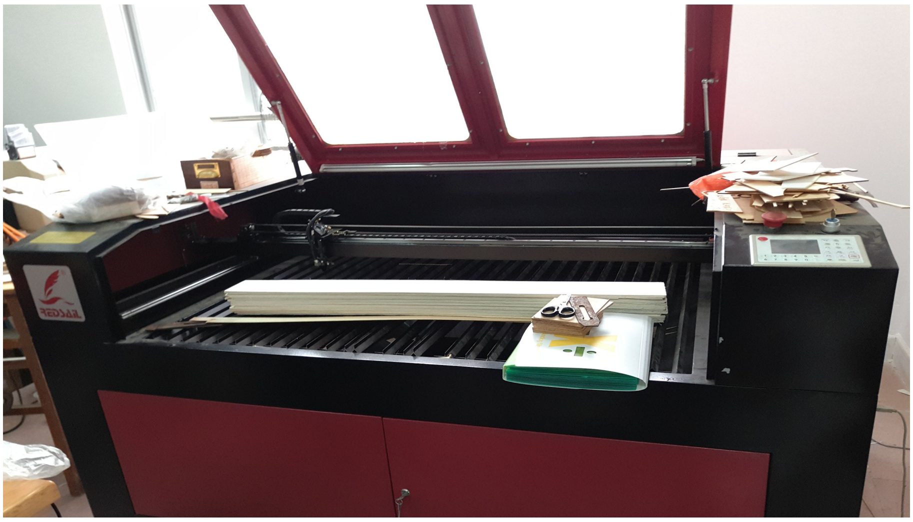

Figure 24. REDSAIL Laser Cutters CM-1690 machine and materials

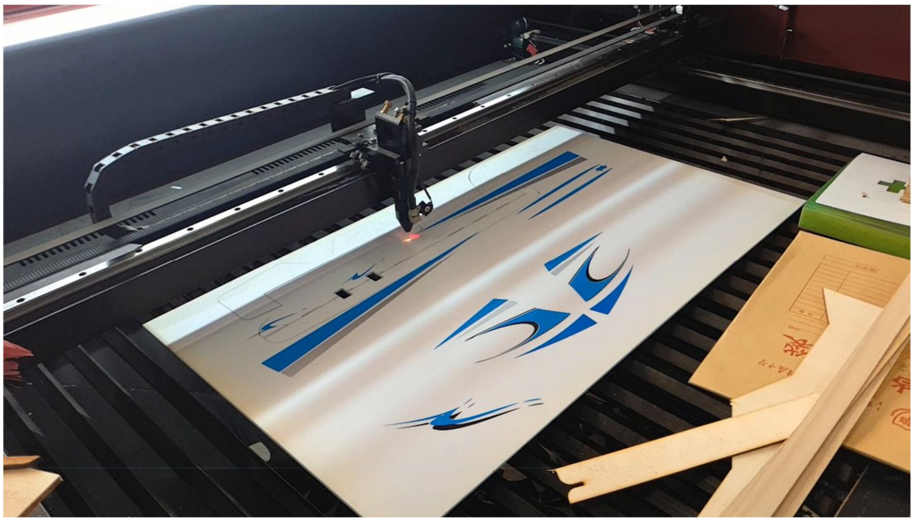

Figure 25. Laser cutting to manufacture the MAV test platform

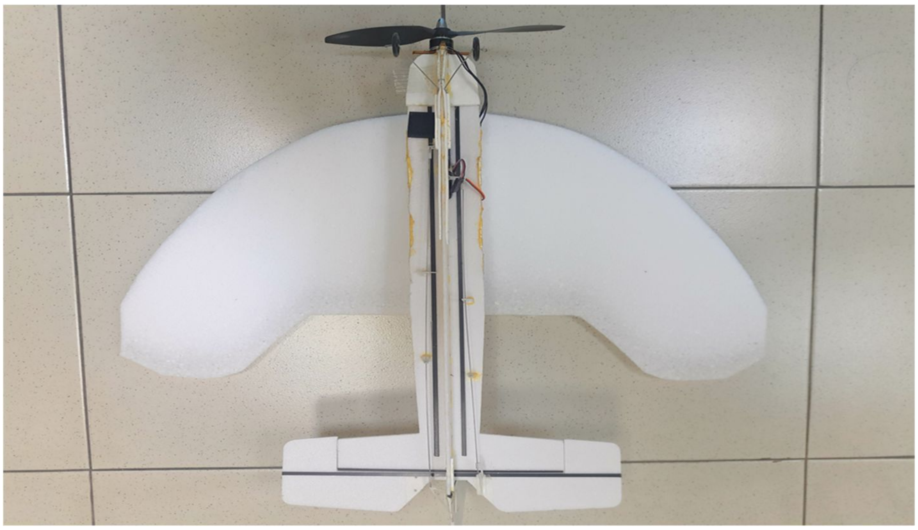

Figure 26. The prototype of Javan Cucumber model after final assembly

III. Results and Discussion

A. Characteristics and Comparison of Results

1) XFLR5

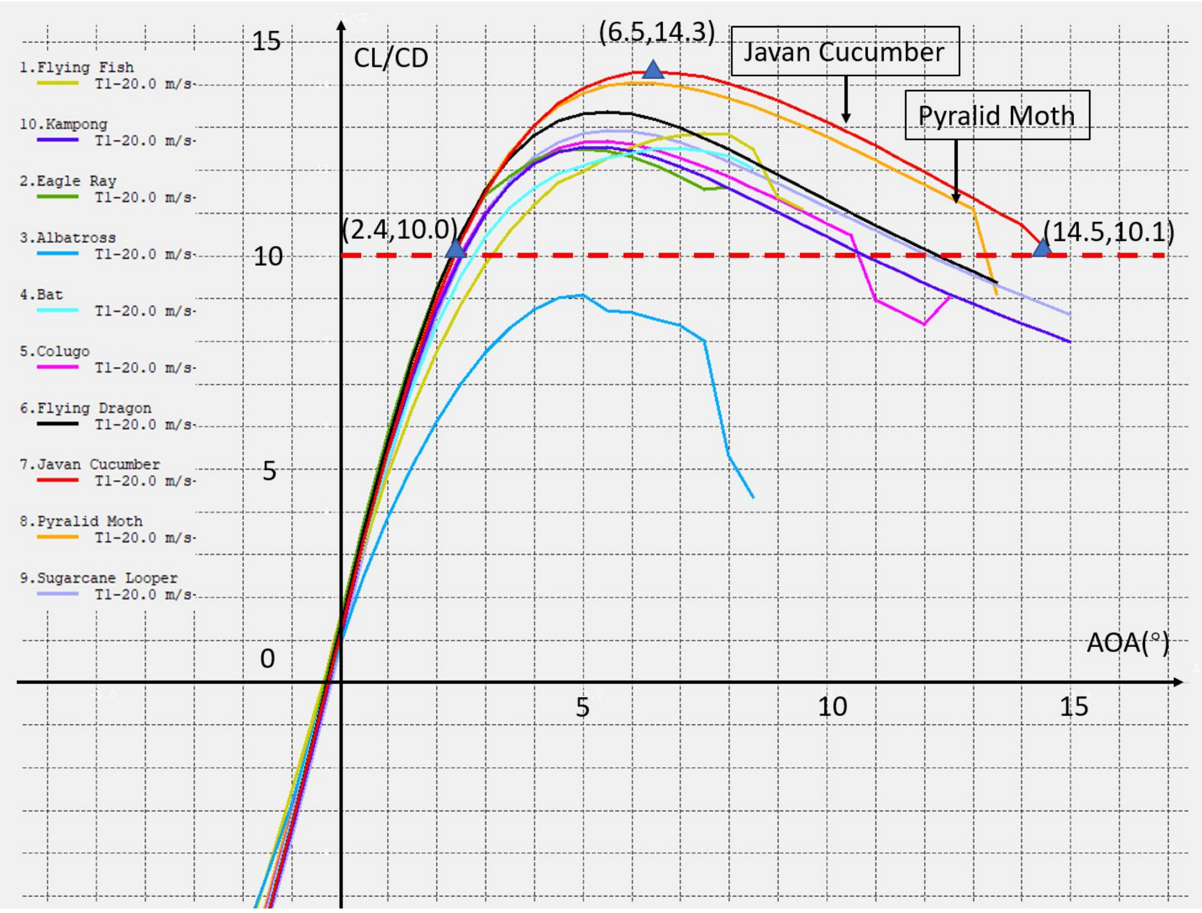

Figure 27. XFLR5 simulated CL/CD results of ten species.

Through XFLR5 VLM analysis, a set of CL/CD data for our 10 tested modes was obtained. From the graph, it is clear that all these 10 models have relatively high CL/CD, which suggested their high flight capabilities. The most significant curve is the one representing Javan Cucumber, which is above all the other curves, indicating that, among these 10 models, Javan Cucumber has the highest CL/CD at any AoA. According to our criteria, having highest CL/CD in a long range of AoA means that it has the best performance among all models.

Moreover, a further analysis on its curve shows that it reaches its highest CL/CD of 14.3 at 6.5 degrees. Since the general working condition for gliders is the AoA being from 3 degrees to 8 degrees, Javan Cucumber will give its best performance when installed on gliders we are currently using.

Furthermore, from the graph, Javan Cucumber also has the widest range of AoAs for which CL/CD is maintained above 10. from 2.4 degrees to 14.5 degrees, the CL/CD of Javan Cucumber is consistently above 10, maintained at a high level. This indicates that Javan Cucumber may still be able to work in less feasible conditions outside the general working condition of 3 to 8 degrees. Hence it is more able to counter the change of conditions due to pressure, temperature and other factors and has the potential to be more widely applied on gliders for a variety of uses in different environments.

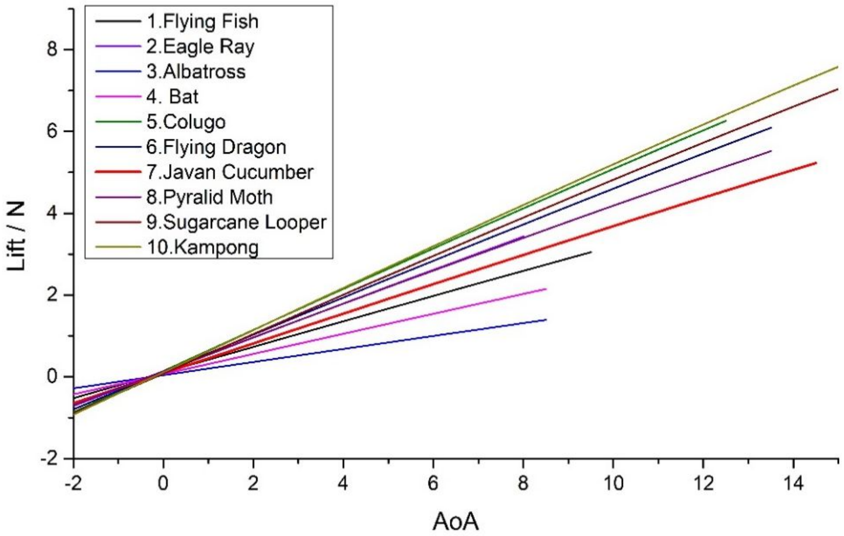

Figure 28. The lift data of ten species from XFLR5.

Along with the CL/CD graph, the lift graph was also generated for analysis. Although in the lift graph Javan Cucumber did not have the highest lift, this did not disqualify our results of the CL/CD graph. When referring to the lift graph, it is not enough to just look at the lift without taking the reference area of the wings into account.

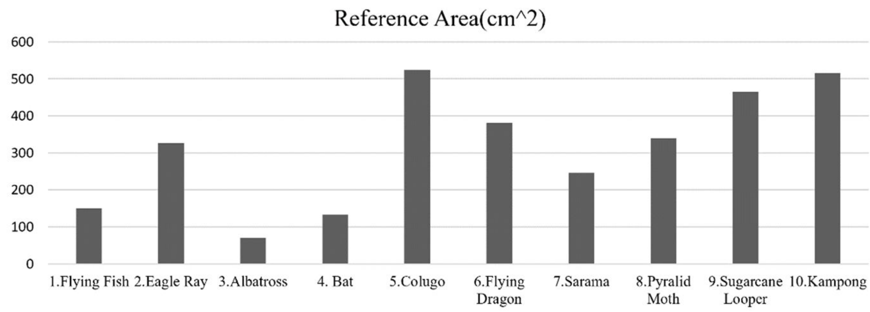

Figure 29. The reference area of ten models

From this diagram, it is clear that Javan Cucumber has the third smallest reference area among all the graphs. Yet, it can generate fourth highest lift with such small reference area. This show that Javan Cucumber is more efficient (in the sense that it can generate more lift with same reference area), hence can save materials and space. Furthermore, the results of the analysis on full-scale Javan Cucumber, which will be shown later in this paper, will prove that in a full scale, Javan Cucumber will generate enough lift for the application.

Using the same criteria, the Pyralid Moth also displayed its high CL/CD in a wide range of AoAs, which is above all the other models (except for Javan Cucumber). Its curve is similar to Javan Cucumber's which means it has all the strengths aforementioned in Javan Cucumber, yet it is not so good as Javan Cucumber. Hence, the Pyralid Moth was determined to be the second best among all the models, other than Javan Cucumber.

2) *ANSYS Fluent*

XFLR5 vs Fluent in CL	XFLR5 vs Fluent in CD	XFLR5 vs Fluent in CL/CD

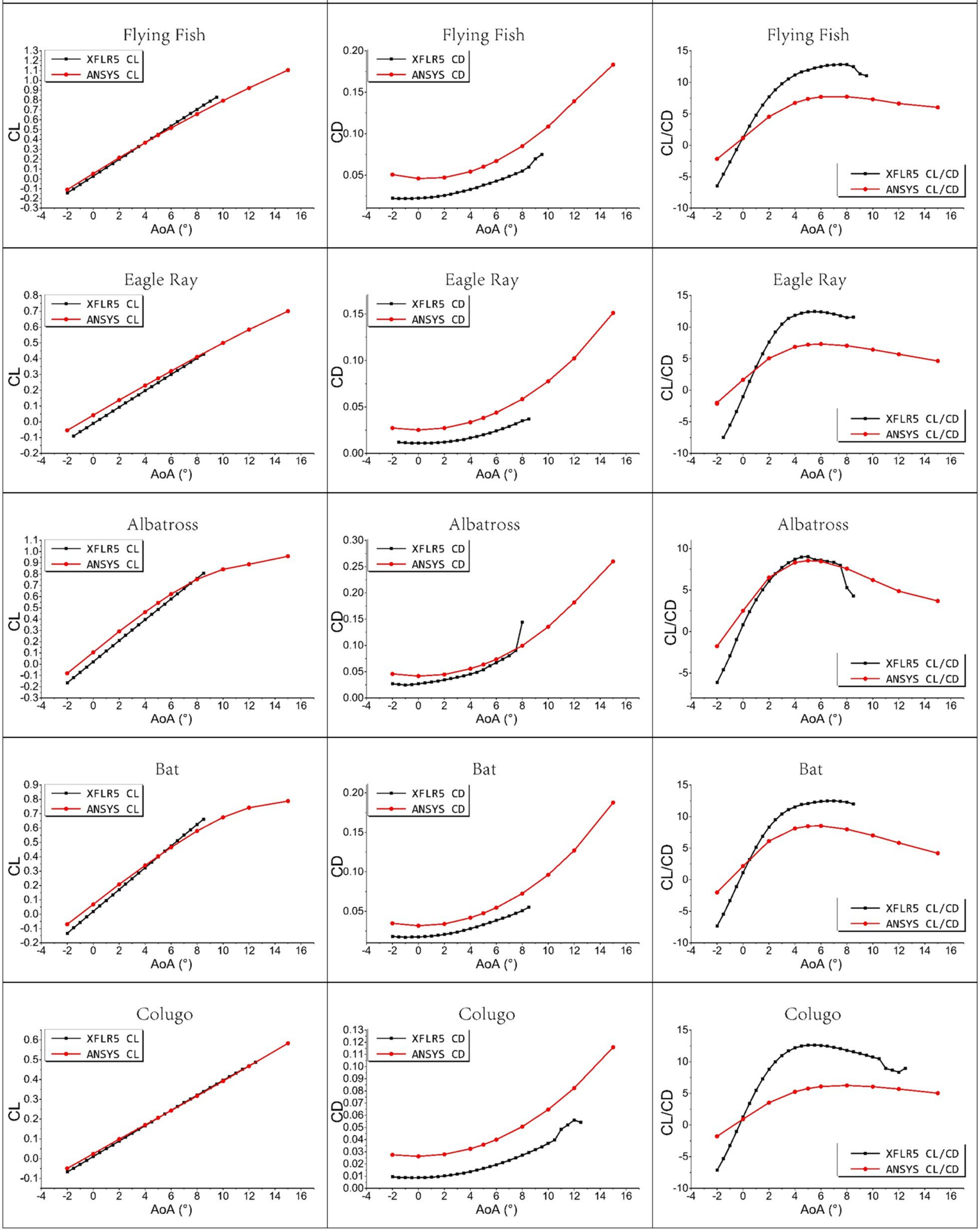

Continued

XFLR5 vs Fluent in CL	XFLR5 vs Fluent in CD	XFLR5 vs Fluent in CL/CD

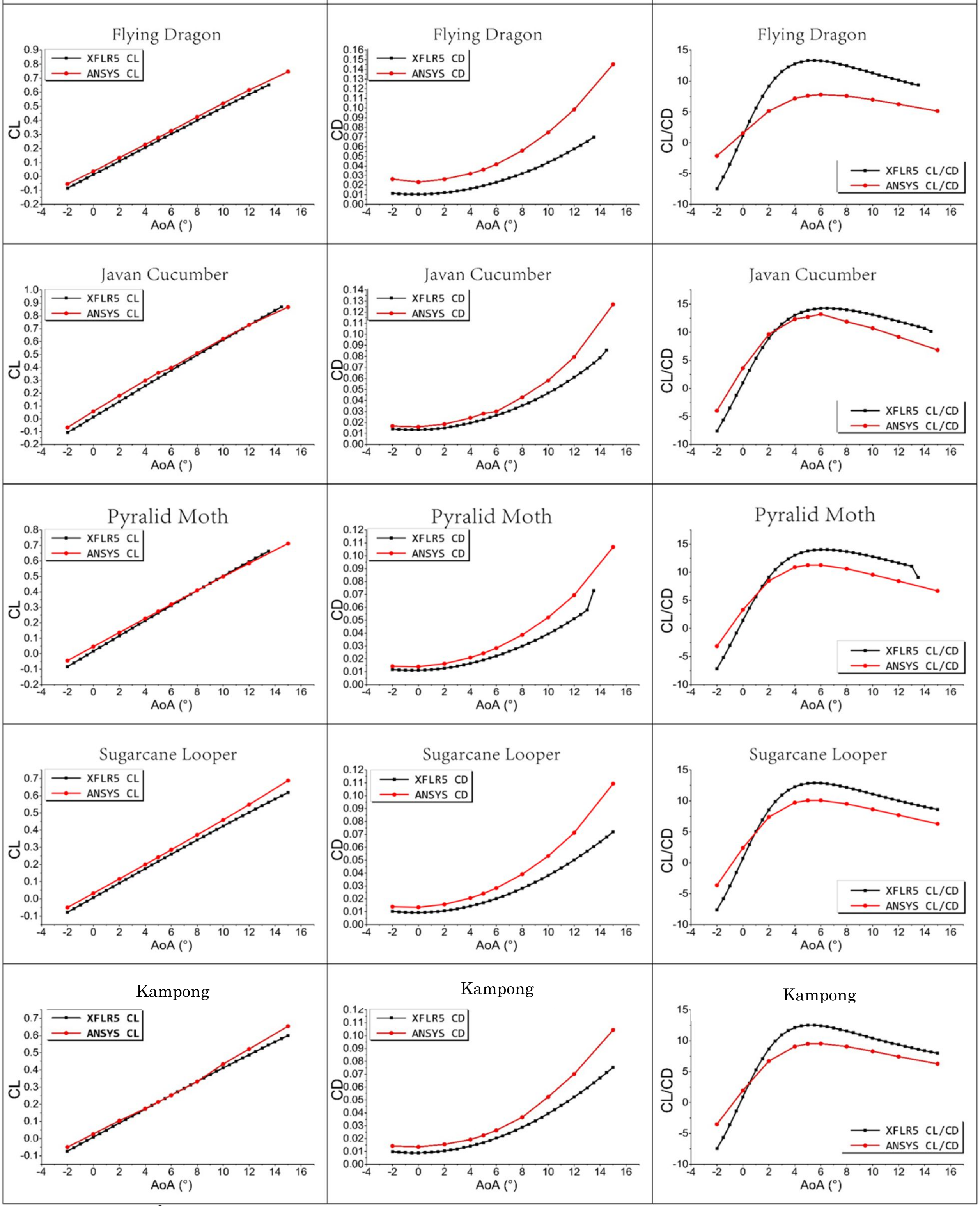

Figure 30. The comparison between 10 models' CL, CD and CL/CD results of XFLR5 and ANSYS

The lift data produced by ANSYS Fluent accurately matched that produced by XFLR5 (refer to Fig.30).

However, the drag data has a small deviation between XFLR5 results and ANSYS Fluent results. Despite this, those two sets of data, after plotting against AoA, show consistent trends. The deviation, which was largely due to the inviscid assumption of Horseshoe Vortex method of XFLR5 in calculating drag. The ANSYS Fluent, however, solves the N-S equations which fully take the viscosity of the air into considerations. In our meshing, the y+ value was also reduced to less than 1 so that the viscous sublayer in the boundary layer was well-simulated. However, the inaccuracy with reference to the deviation can be considered acceptable as all the results were affected to the same extent due to the same limitations of the algorithms used.

More importantly, two software both suggested that Javan Cucumber and the Pyralid Moth were the top 2 performing species, which corroborate the selection of the best performing species based on XFLR5 results. The selection was thus verified to be convincing[20], which made our comparison reasonable and reliable.

3) Pre-Validation of Wind Tunnel Results Using NACA 0012 Wing Section

Generally, the data collected from the pre-validation gave credits to the precision and usefulness of the results from the wind tunnel experiments. As shown in Fig. 31, the CL data we obtained shown coherent trends with the existing literature. From the existing literature, the linear region of CL for NACA 0012 is 2-10° AoA under Re 50000-100000. In this region, the results from our wind tunnel pre-validation also demonstrated good linearity. However, the results with same trends may not accurately match each other. We account this discrepancy to a systematic percent error, which will be further discussed later. Nonetheless, the percent error for CL was constantly 55%, which indicates that the results from wind tunnel tests were usable but warrant considerations.

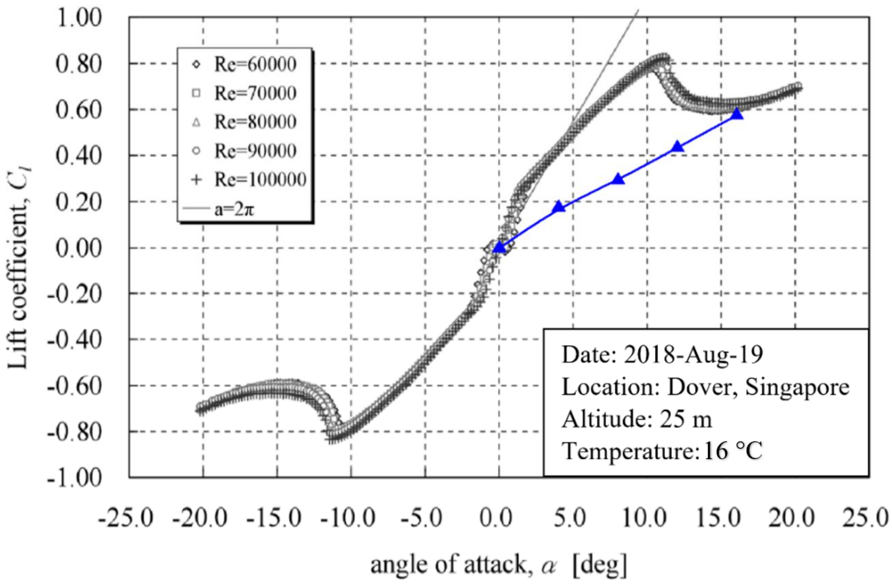

Figure 31. Comparison between the Cl of NACA 0012 from existing literature and wind tunnel

Additionally, as shown in Fig. 32, the CD data also had an identical trend with the existing literature. The CD results below stall angle also suggested a uniform systematic error of 60%. Thus, the drag obtained from the wind tunnel was also usable if we take the constant systematic error into consideration. However, the drag beyond stall angle was indicated to be largely inaccurate. The reasons of this inaccuracy will be further discussed in Chapter IV.C. Despite this, the focus on the performance will be in the normal working conditions, in which the AoAs were below stall angles. Thus, as the region of inaccurate drag was out of the scope of comparisons, the inaccuracy of the drag beyond stall angle will not affect the usefulness of the wind tunnel data.

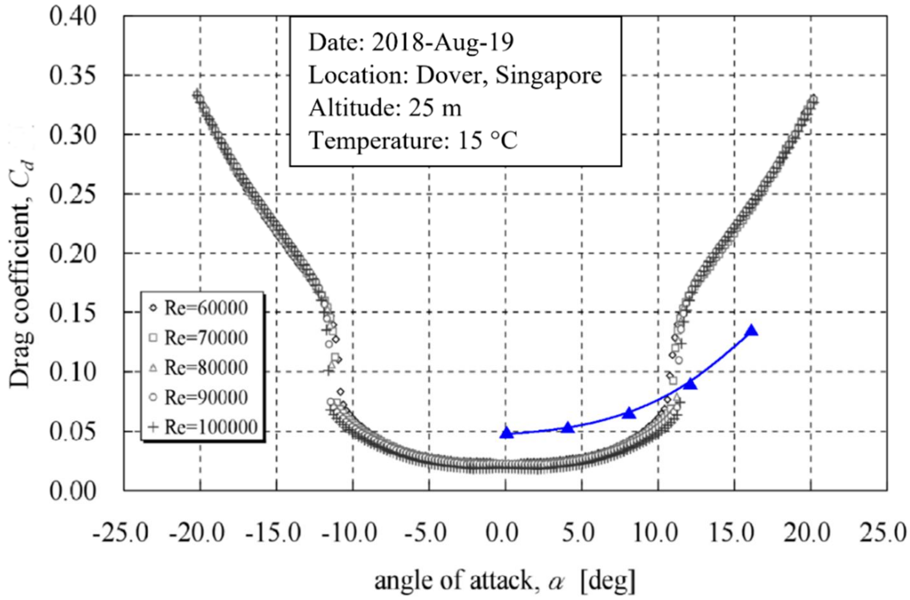

Figure 32. Comparison between the Cl of NACA 0012 from existing literature and wind tunnel

Overall, the pre-validation had proved the reliability and precision of our wind tunnel results. Yet it also informed us about an ever-existing but uniform percent error. A more prudent view on the results of later actual tests was then necessitated and implemented throughout the analysis of wind tunnel results.

4) Wind Tunnel Experiments

By comparing the three sets of CL results of Javan Cucumber in Fig. 33, it can be observed that the CL curve initially fits well with the CFD curves, at low AoA. As AoA increases, at around 6 degrees, however, the wind tunnel CL results start to deviate from the CFD curves, being smaller than CFD CL values. It thus can be inferred that the occurrence of boundary layer separation and other factors may lead to the deviation. This will be discussed later. Generally, the trends of these three curves are the same: CL increases linearly with AoA.

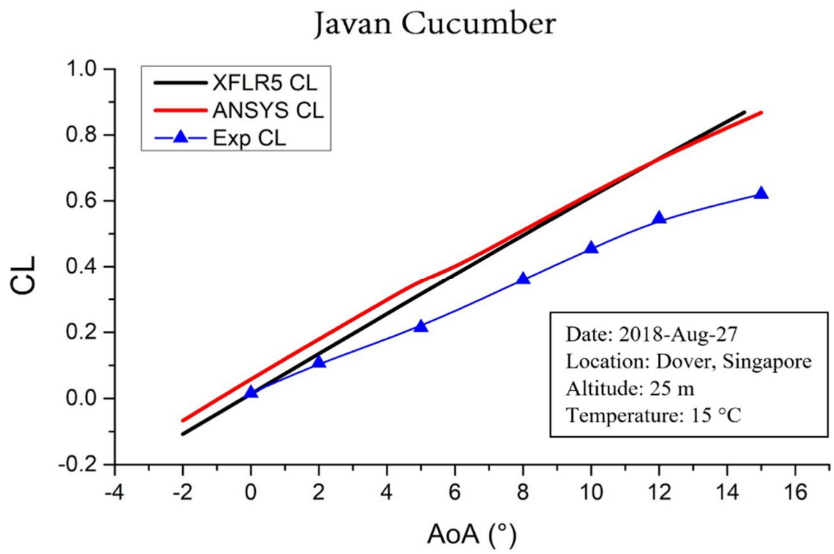

Figure 33. Comparison of the Javan Cucumber's CL from the CFD and wind tunnel experiments.

Similar to the CL graph, the absolute CD values of wind tunnel data deviate from the CFD data after around 6 degrees, becoming higher than the CFD data (Fig.34). This can also be explained by the occurrence of boundary layer separation. The trends of three CD curves were also similar, which increased with AoA at an increasing rate.

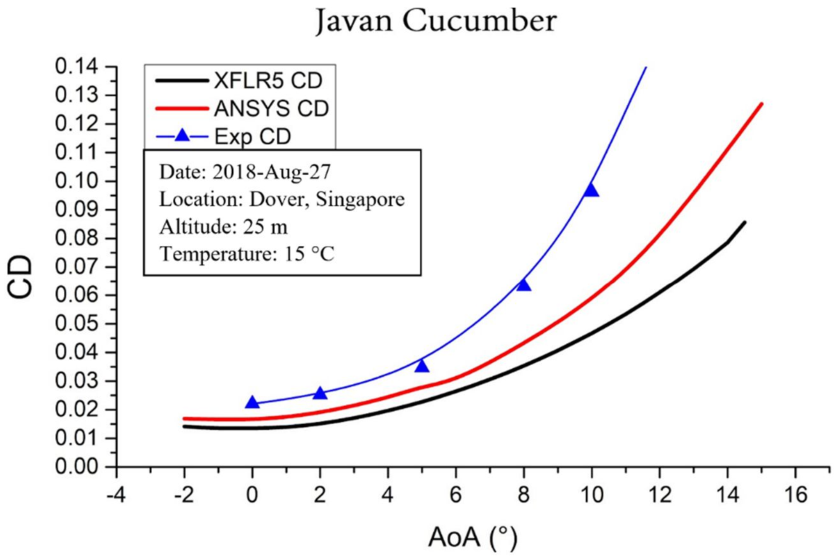

Figure 34. Comparison of the Javan Cucumber’s CD from the CFD and wind tunnel experiments.

When coming to the comparison of CL/CD data in Fig.35, it can be observed that the wind tunnel CL/CD data generally had smaller values than those of ANSYS and XFLR5 data, as the CL/CD curve of wind tunnel was always below the CL/CD curves of ANSYS and XFLR5. As aforementioned, the CL data of wind tunnel being lower than CFD data, and the CD data of wind tunnel being higher than CFD data, surely the CL/CD data of wind tunnel will be lower than CFD data. However, the difference between the wind tunnel CL/CD and the CFD simulations was observed to be uniform for every AoA, being around 7.5. Hence, it can be inferred that there were systematic errors that lead to a smaller value of wind tunnel CL/CD. Despite this, the trends of all these three curves were the same: CL/CD first increases, reaches its maximum point at around 6 degrees, and then decreases at a slower rate.

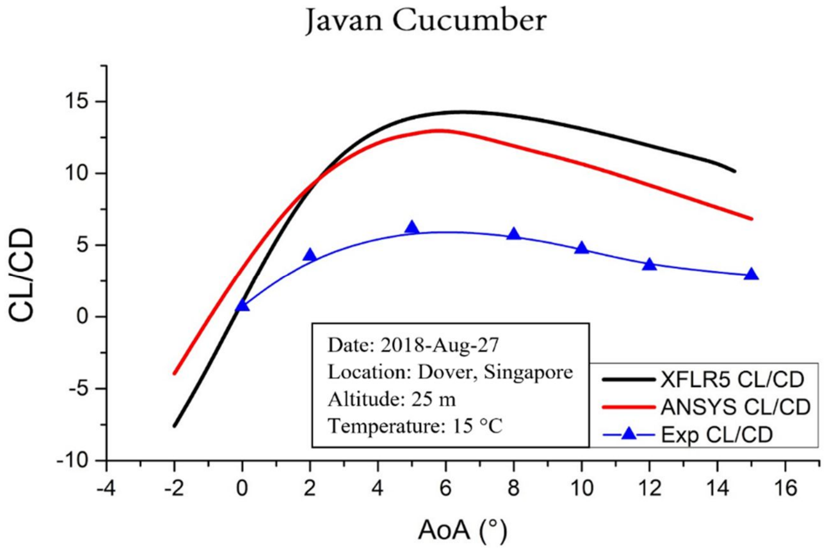

Figure 35. Comparison of the Javan Cucumber’s CL/CD from the CFD and wind tunnel experiments.

Since all three sets of data, both CL, CD and CL/CD from two kinds of computer simulation and an actual experimentation, all show the same trend, the results of Javan Cucumber we obtained from the computer simulations were validated by the experiment. Since the accuracy and reliability of our computer simulation methods, both XFLR5 and ANSYS, have been proven by the experiment, the selection of Javan Cucumber as the best model which was based on the results of simulation that it has high CL/CD in a wide range of AoA and high lift, is justified.

A similar comparison between the 3 sets of CL, CD and CL/CD data of the Pyralid Moth, from XFLR5, ANSYS and the real experiment, was also carried out. Similar to the case of Javan Cucumber, the CL and CD data of the Pyralid Moth also start to deviate from the CFD results after AoA 6 degrees, indicating that the boundary layer separation and other factors also had impacts on the accuracy of data collected (refer to Fig. 36-38). However, despite this deviation, the experiment results of the Pyralid Moth had the same trend with CFD results. Hence, the results of the Pyralid Moth we obtained from computer simulation were also validated, and our initial selection of Javan Cucumber being the best model, and the Pyralid Moth being the second best model, was valid.

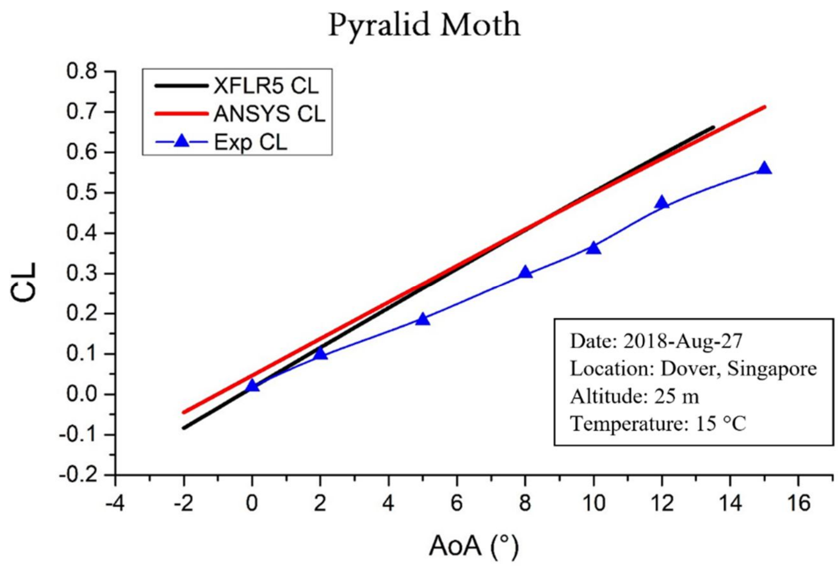

Figure 36. Comparison of the Pyralid Moth's CL from the CFD and wind tunnel experiments.

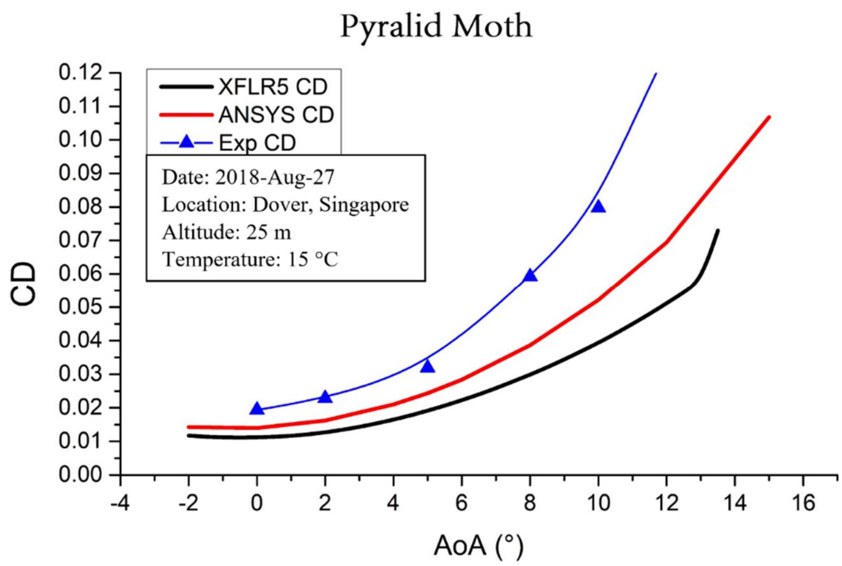

Figure 37. Comparison of the Pyralid Moth's CD from the CFD and wind tunnel experiments.

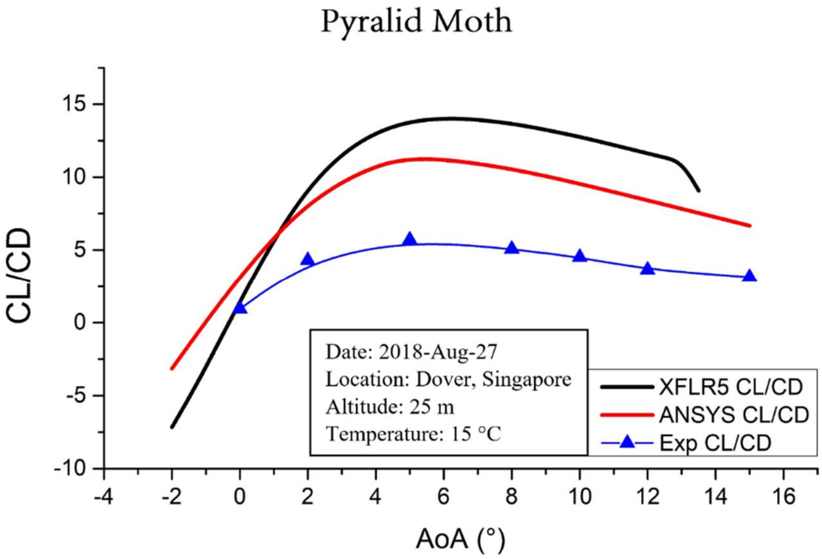

Figure 38. Comparison of the Pyralid Moth's CL/CD from the CFD and wind tunnel experiments.

5) Reasons for Discrepancy between Wind Tunnel and CFD Results

The discrepancy between wind tunnel results and CFD results may come from multiple factors.

First, as aforementioned, the boundary layer separation may be the most profound factor. For both Samara and Pyralid Moth, their CL and CD wind tunnel data initially fitted well with the CFD data, in small AoAs. However, as AoA increases, after 6 degrees, they deviate from CFD curves, either becoming bigger or smaller. As the computer simulation already showed that stall of both wings starts from AoA 6 degrees, it can be inferred that the stall caused the deviation of the wind tunnel data, both CL and CD data, from the CFD data. Since the separation is where the bubble detaches from the wing and the laminar flow becomes turbulent, CFD simulation itself may not give accurate data under stall conditions. On the other hand, in wind tunnel experimentation, since the lift and drag forces were changing drastically when stalling, sensors may not be able to collect accurate data. Additionally, the elasticity and damping effects of the metal rod and the model also helped to reduce the effects of a larger but vibrating drag when stalling. Therefore, the occurrence of stall in high AoAs may lead to the inaccuracy of both CFD and wind tunnel data and hence contribute to the deviation of both curves from each other.

Moreover, the wind tunnel experiment consisted of multiple parts, which could all contribute to the discrepancy and their effects may add up. For example, the force sensor in the wind tunnel may possess its own systematic error in measuring the forces. The wall effects which reduced the velocity of flows near the walls. This effect reduced the real Re number of the flows near the walls, which deviate the actual results with real ones. The turbulence in the wind tunnel may also introduce interference to the flow over the models.

Although the test models were well-polished until reaching mirror-like surfaces, there would still be invisible defects on the surfaces, which made the airflow deviate from that of perfect surfaces. The positioning of the rod, however, was not at the CP where the aerodynamic forces directly acted on. The measurements may thus not be accurate. The rod in the wind tunnel also introduced interference with models' flow, which further deviate the results.

Therefore, as the result of a multitude of factors, there was an ever-existing systematic error of a constant percentage before stalling. After stalling, the inaccuracy of both wind tunnel and CFD results were also expected to be higher. This also informed us the necessity of holding a prudent view on the accuracy of both experimental and simulation results.

B. Comparison between full-scale Javan Cucumber and Conventional Designs

1) Testing of the Full-Scale Models Using ANSYS Fluent

- Analysis

Compared with the current commercially available powered glider, such as XT912 Tundra-Merlin [21] with a 10.0 m wingspan, both data and graph showed that Javan Cucumber has a slightly lower CL/CD polar curve and greater drag (refer to Fig.39&41).

However, the lift that the Javan Cucumber can generate at the speed of 20ms^{-1} was about 40% in average greater than the lift that the XT912 can generate at the same AoA (refer to Fig.40). It could even generate a lift of 2521N under 5.4° AoA. This allows the model to carry theoretically 257.0 kg of loads. Hence, the greater drag is acceptable given this model's advantage in lift force. Meanwhile, the Javan Cucumber still maintained a high CL/CD over 10 in a broad range of AoA of 1.3° to 12.8°, with a relatively large lift force.

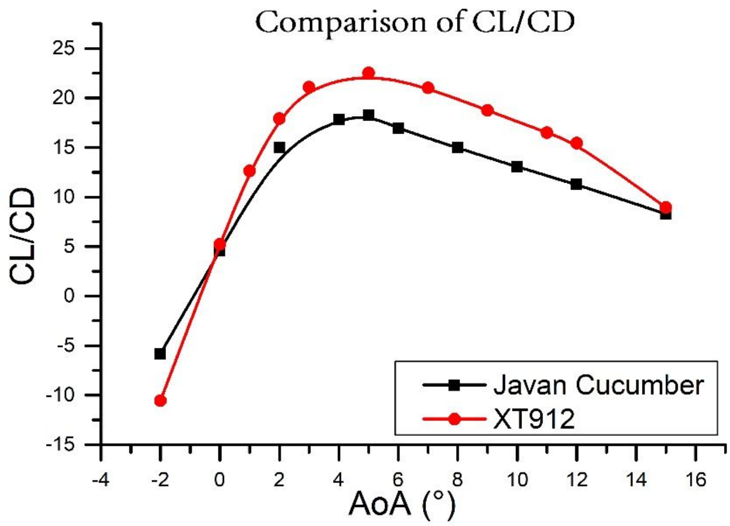

Figure 39. Comparison of the CL/CD between Javan Cucumber and XT912

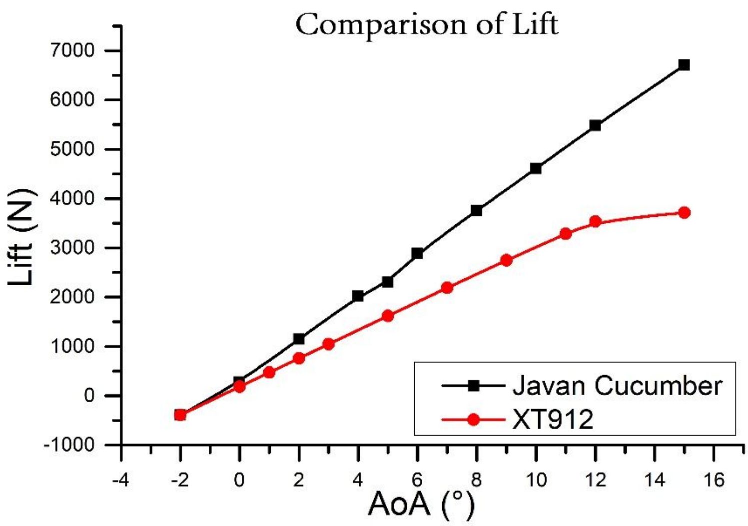

Figure 40. Comparison of the lift between Javan Cucumber and XT912

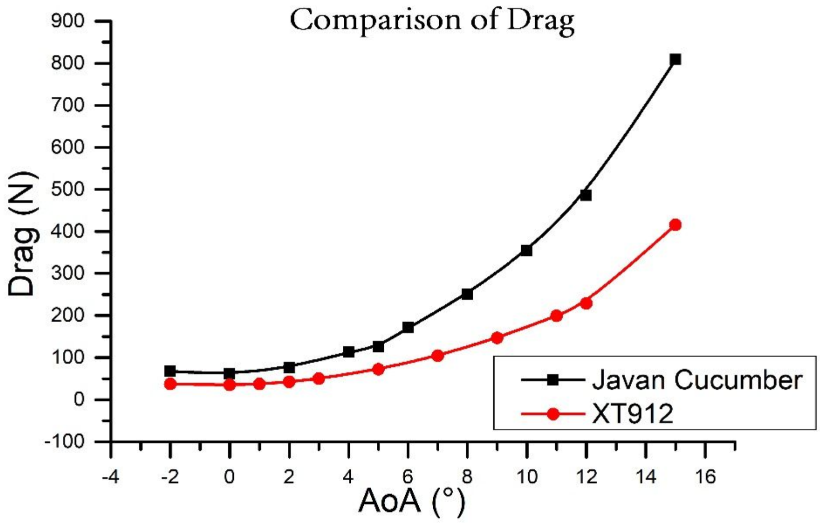

Figure 41. Comparison of the drag between Javan Cucumber and XT912

The lower CL/CD ratio of the Javan Cucumber was mainly due to a larger drag. This is also observed in Fig. 40, in which the drag-AoA graph of Javan Cucumber was higher than that of XT912. The larger drag may be a result of the greater wing area of Javan Cucumber, which in the meantime also increased the lift of the model.

Thus, the Javan Cucumber had the potential to undergo aerodynamic shape optimisation so that it may outperform the currently used wing models for powered gliders by reducing its drag. However, we did not have the specific knowledge on the aerodynamic shape optimisation. This hindered our progresses for an improved biomimetic model with lower drag which could outperform the conventional designs in term of CL/CD.

2) Testing Prototype on MAV

The testing of the prototype on an MAV test platform both indoor and outdoor was successful. The venues are shown in the Fig. (42.43.44) The plane took off at a slower speed from the ground. It required less throttle to maintain its altitude in level flight compared to that with conventional wings. It also hovered with little loss in speed when turning, which suggested that the increase in drag only had a small impact on its overall performance. The success of this trial showed the great potential of Javan Cucumber to be further studied and commercialised.

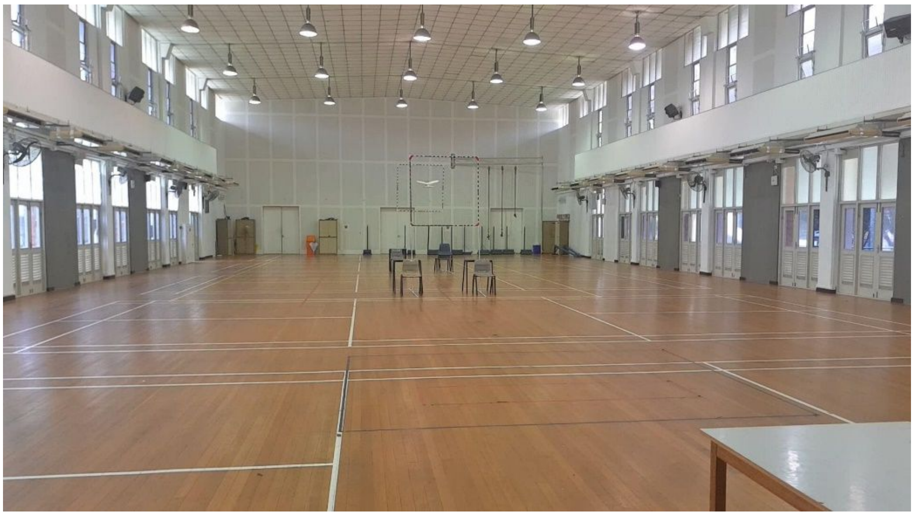

Figure 42. Indoor Prototyping Test Venue 1 (Indoor Sports Hall, Temasek Junior College)

Figure 43. Indoor Prototyping Test Venue 2 (Indoor Sports Hall, Dunman High School)

Figure 44. Outdoor Prototyping Test Venue 1 (Centre Garden, Dunman High School)

IV. LIMITATIONS

A. XFLR5

In XFLR5 testing, due to the limitations of the Xfoil algorithm, we did not manage to fix the problem that some points could not be interpolated in the Xfoil direct analysis e.g. for the Albatross model, Span pos= 0.07m, Re=3333, CL=-1.18 could not be interpolated. As a result, it was observed that the results of some models at high AoAs did not converge, result in a vacancy for their XFLR5 results at high AoA. This error is because we have reached the limits of the 2D approximation for the viscous drag, and therefore the fixed Cl type of analysis could not help to interpolate the CD values.

Moreover, in VLM, the calculation of the lift distribution, the induced angles and the induced drag was inviscid and linear. Therefore, the viscous drag caused by air cannot be directly calculated out but rather interpolated from the lift force and lift coefficient which can be directly calculated in VLM. This resulted in an underestimation of drag variables.

Lastly, the automatic mesh applied in VLM was crude, which made the calculation of lift and drag less accurate. The number of mesh elements generated in a mesh in VLM was only around 641 (displayed by the software). Since the mesh element number was very low, the calculation based on the mesh may not be able to give very accurate data.

B. Fluent

Although the Fluent is an industrial level CFD software, there were still its limitations affecting the accuracy of results. According to the error theory, there are unavoidable errors between simulation results and the real value. In our simulations in Fluent, we strived to minimise these errors but unable to totally remove them. One of the most profound ones was introduced by the imperfect meshing, where our lack of experiences may induct an error in the result. Some of our models may contain sharp wingtips, where we failed to generate hexahedral cells. We thus separated the tips with the main wings to mesh it independently. Tetrahedral cells were then introduced in these wingtips, and the results generated based on it may not be accurate as those from hexahedral meshes.

The reduced meshing quality had an observable impact on the residuals. Typically, the industry accepts a result with residuals smaller than $1e^{-6}$ as an accurate one. However, in our calculation, the typical residuals for scaled models were in the magnitude of $1e^{-4}$ after 200 iterations. Despite this, we could observe in the force monitors that the results had already converged. Thus, the higher residuals may not have a significant impact on the accuracy of results. To make the simulation more convincing, we have improved the meshing quality on the full-scaled models by reducing the number of tetrahedral-occupied cells. This improvement greatly reduced the residuals to the magnitude of $1e^{-9}$ after 1000 iterations, which was considered as a very accurate result.(Fig. 45)

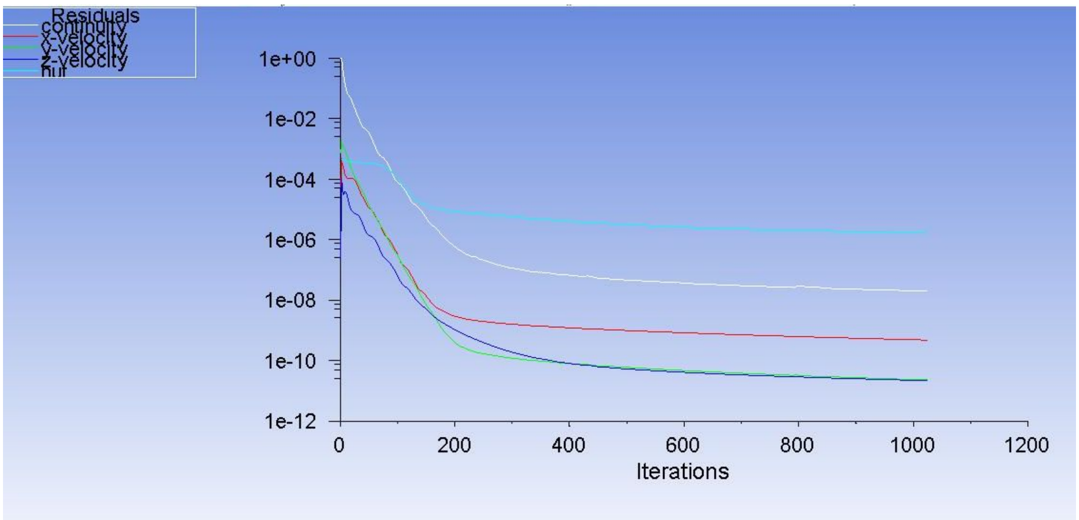

Figure 45. Residuals of Javan Cucumber Full Model After 1000 Iterations

Another limitation of our results was the application of the one-equation S-A turbulence model. Due to the lack of computing power, S-A model as a fast choice was selected. Compared to other two-equation counterparts, the S-A model only solved one turbulent transport equation, namely the turbulent kinetic energy. However, the two-equation models have also taken the turbulent dissipation ε, or the Specific turbulence dissipation rate ω, into account. The neglection of these quantities may result in a less accurate result.

C. Wind Tunnel Experiments

The models used in the wind tunnel experiment had its own limitations. As aforementioned in chapter II.G.3, although the surfaces of the model were carefully polished, there is still roughness of the surface that may affect the accuracy of the data. In CFD simulation, it was assumed that the surface is absolutely smooth. Hence, the drag data from wind tunnel experiment will be higher than the theoretically calculated drag value, and the lift may be affected as well. Additionally, the Pyralid Moth model was not 3D-printed out in a whole part but was made by gluing three separate parts together. Hence, the small gaps between the parts may contribute to inaccuracy of the data collected in the experiment.

Moreover, the wind tunnel used in this experiment is an educational wind tunnel, which has some limitations like high systematic errors in force sensors and relatively high turbulence in the wind tunnel. These limitations can affect the accuracy of data collected.

Lastly, the set-up of the experiment may also have problems. The AoAs were altered by rotating the plate with degree markings. However, the markings were difficult to read, hence it was difficult to ensure that the AoAs were exactly the ones we wanted to set up. Furthermore, the half wing models were attached to the sensors by a relatively long metal rod which may bend during the experiment and therefore change the actual AoA. Although a stainless-steel rod was used to ensure its hardness, the rod may still bend slightly. Moreover, the half model was set up in the way that the distance between the model and the walls was short, due to the small size of the testing part of wind tunnel. Hence, the interference of wall effect on the data collected, as aforementioned in Chapter III.A.5, may be significant.

D. Prototyping

The comparison between the prototype and conventional wing was largely qualitative in this research. This was due to the lack of tracing devices of the plane in 3D space. Without any flight logger on board, we were unable to collect its flight data and thus no quantitative analysis can be done. However, there were only military level devices which were capable to trace an aircraft of the similar size to our prototype. Staying inaccessible to that equipment, this research was confined to a qualitative comparison between conventional wings and our biomimetic design.

The surface roughness brought by the CNC milling on EPP material was also a limitation. The great roughness could induce a larger drag, which may impact the flight performance of the prototype. However, the EPP is soluble in most of the solvents so coating any materials on the surface was impractical. It also contracts when heating, which made surface laminating impractical.

The actual flying tests faced many issues too, due to the complicated situation in the actual flying. A little problem with the gear may lead to the failure of the test. The indoor tests showed the high potential of the model, however, the outdoor tests were severely affected by the environment and the control surfaces (especially ailerons) were found hard to be manoeuvred properly at the outdoor venues. This led to another problem that our MAV went haywire and crashed into a tree once. The plane was hence damaged to a small extent. Although we tried our best to repair the model, there were still differences in the plane’s performances before and after the crashing. Such differences might lead to observable differences in the final results. Moreover, there were much more variables to be controlled in the actual flying tests than the simulation in CFD software while many of the variables were difficult to be controlled firmly. These variables not only existed in the materials and parts that the plane utilised and the actual flying environment, but also come from the human error in controlling the plane and inconsistency under actual flying condition. Therefore, even a rigorously qualitative analysis was difficult to be done. An accurate quantitative test of the prototype was thus more unapproachable.

V. Conclusion and Recommendation

In conclusion, the hypothesis was proven to be true: Javan Cucumber performs the best among all the selected species as It can sustain high CL/CD across a wide range of AoA, and produce enough lift force at full-scale. This excellent performance is because the Javan Cucumber features elliptical wings and can experience constant lift under different AoA. Besides Javan Cucumber, we also found the models of the Pyralid Moth performed well in the simulation and testing.

In comparison with the existing wings for motor gliders, our best model Javan Cucumber has comparable or even better aerodynamic performance. That is, when AoA is 5.4°, the Javan Cucumber model can carry theoretically 257 kg of mass under a low speed of $20ms^{-1}$ while the XT912 Tundra-Merlin can only carry 223 kg of mass at the same speed. Although this is mainly because of the bigger reference area of Javan Cucumber, such design features can still possibly be applied in future power glider designs.

Despite current achievements, there are some improvements that could be made in this research in current methodology. As this study was done only on representatives for respective groups of similar structures, further studies could be done to investigate similar plant structures of the Javan Cucumber and Pyralid Moth to identify a more ideal structure. Moreover, for CFD simulation, the mesh can be further improved to ensure more accurate results. Additionally, for the validation of CFD results using wind tunnel, a professional wind tunnel could be used which has less turbulence and is able to conduct more accurate measurement.

Furthermore, the scope of this research could be wider. Further studies could be done to investigate the stability and manoeuvrability of such structures as such attributes would also be important to flight, especially in the context of future traffic. The geometry of these designs can be further explored in other personal air vehicle development aided by the future improvement of the technologies, such as thrust vector control engine, new material like aerogel and full-scale 3D printing. All these revolutionary technologies can be utilised in our designing process to create more efficient powered gliders or other flying vehicles.

VI. NOVELTY OF RESEARCH

A. The Use of Biomimicry

Currently, wing design is usually done by calculations which are guided by control theory. This may lead to the loss of innovation, as our research shows that innovation in the field of wing design is inhibited by factors like the over-reliance on theoretical calculations and too much focus on analysis [22]. This indicates that if we follow this way, we may not get enough inspiration to come up with a satisfying wing design. Therefore, instead of adopting the conventional way, we choose another one, biomimicry, an approach to innovation that seeks sustainable solutions to human challenges by emulating nature's time-tested patterns and strategies. Successful cases in aerodynamics, like bullet trains inspired by Kingfisher birds, show that biomimicry can work. Therefore, in our research, biomimicry is used to seek more inspiration from the wings in nature and modify them for our uses.

B. Extensiveness of Studying

In order to find the best biomimetic wing design for gliders, we studied the features of a variety of species in the nature, both plants and animals. Out of all flying or gliding species, we finally identified ten of nature’s most notable flyers and examined their structures. The ten species chosen for study are Atlantic Flying fish (Cheilopogon melanurus), Spotted Eagle Ray (Aetobatus narinari), Albatross (Diomedeidae), Malaya Colugo (Galeopterus variegatus), Golden-capped Fruit Bat (Acerodon jubatus), Flying Dragon (Draco Volans), Javan Cucumber (Alsomitra macrocarpa), Pyralid Moth (Sufetula diminutalis) Sugarcane looper (Mocis frugalis), Kampong (Oroxylum indicum) (Fig.3).

C. Robustness of the Conclusion

The conclusions we drew from the investigation were believed to be robust. This is because this research was done in a thorough manner. In this research, two CFD simulation software of different algorithms were utilised and we used their results to corroborate with each other. If the results from two software matches and selections of the best performing species based on two software’s results are identical, the simulation results were then proved to be convincing. However, the CFD results were not fully trusted in the industry. We then conducted wind tunnel tests to validate our CFD data. After the simulations and experimental tests, the performance of our models, especially the best ones, were thoroughly examined. To show the utility of the best model, a full-scale simulation was conducted and its performance was compared with the most popular conventional model. Only if our full-scale model outperforms the conventional one according to the reasonable criteria, its potentials to be applied in the aircraft industry can be suggested. Moreover, previous selections and comparisons are either computational or experimental, without a physically observable indication of the model’s excellence. Hence, a practical test of the prototype of the new design is necessary and vital. By visually observe the satisfactory flying capabilities of the new design in the sky, we can finally conclude that the best biomimetic model owns its excellence suggested by those simulations and wind tunnel tests. The final conclusions drew in Chapter V are then robust and convincing.

Comparing to usual approaches, the cross-verification of the two CFD software made the selection of the best species more convincing. The comparison between full-scale models also indicated the applicability of our designs in the aircraft industries. Moreover, the prototyping of the best model gave this research practicality, making it move a step forward from pure theories and experiments.

VII. ACKNOWLEDGEMENT

First and foremost, we would like to thank Dr. Victor Wang Peng Cheng of Singapore Institute of Technology, our mentor, for providing insights and expertise on CFD, as well as giving comments that greatly improved our manuscript. We would also like to thank Mr. Khoh Rong Lun of Temasek Junior College and Mrs. Jeanne Wan of Anglo-Chinese Junior College for their unwavering support and invaluable guidance through this year-long project. In addition, we would like to give special thanks to Dr. Dimitrios Chua Khim Heng for his patient guidance and assistance throughout the experiment session of our research. We would also like to thank Mr. Jeggathishwaran S/O Panisilvam for his enthusiasm to assistant us use the work station at SIT to run the Fluent simulation. Last but not least, we are grateful for all the teachers, seniors and peers who gave comments and provided kind helps to us in this long journey, both online and offline.

Wang Jiwei mainly contributed to the identification and selection of the species that this project studied. He also worked on the planform sketching in AutoCAD and XFLR5 simulations. In addition, the ICEM CFD meshing was mainly done by him and he prepared most data analysis forms. Wang Yiyang mainly contributed to the constructing of 3D models in CATIA and 3D printing for models being used for the wind tunnel experiments. Yiyang also studied the algorithm of Fluent and were in charge of the data presentation using Origin. Zhang Haoyu mainly contributed to the study of algorithm behind XFLR5 and was in charge of simulations run in Fluent. Yiyang and Haoyu worked together to conduct the wind tunnel experiments. Jiwei and Yiyang worked together to construct the MAV platform and did the flight test at Temasek Junior College and Dunman High School. The entire team worked together to write this research paper.

VIII. REFERENCES

[1] "Uber Elevate." Uber Elevate | The Future of Urban Air Transport. https://www.uber.com/info/elevate/.

[2] "EHANG 184." EHANG|Official Site-EHANG 184 autonomous aerial vehicle. http://www.ehang.com/ehang184.

[3] "Powered hang glider." Powered hang glider https://en.wikipedia.org/wiki/Powered_hang_glider.-_Wikipedia.

[4] McMasters, John. A Legacy of Sustaining Innovations in Biomimetic Aircraft Design and Engineering Education. PPT.

[5] Mueller, T. J. Fixed and flapping wing aerodynamics for micro air vehicle applications. Reston, VA: American Institute of Aeronautics and Astronautics, 2001.

[6] Barrett, Ronald M., and Cassandra M. Barrett. "Biomimetic FAA certifiable, artificial muscle structures for commercial aircraft wings." Smart Materials and Structures 23, no. 7 (2014): 074011. doi:10.1088/0964-1726/23/7/074011.

[7] Marks, Christopher R., James J. Joo, and Gregory W. Reich. "A Reconfigurable Wing for Biomimetic Aircraft." 54th AIAA/ASME/ASCE/AHS/ASC Structures, Structural Dynamics, and Materials Conference, 2013. doi:10.2514/6.2013-1511.

[8] Simons, Martin. Model Aircraft Aerodynamics. Chris Lloyd Sales & Marketing, 2000.

[9] Antony Jameson, Thomas V. Jones. "Airplane Design with Aerodynamic Shape Optimization." PPT.

[10] Socha, John. J., and Michael LaBarbera. "Effects of size and behaviour on aerial performance of two species of flying snakes (Chrysopelea)." Journal of Experimental Biology 208, no. 10 (2005): 1835-847. doi:10.1242/jeb.01580.

[11] Mark Drela, and H. Youngren. XFLR5 v6.02 Guidelines: Analysis of foils and wings operating at low Reynolds numbers. PDF. February 28, 2013.

[12] "Similitude requirements and scaling relationships as applied to model testing." NASA. https://ntrs.nasa.gov/search.jsp?R=19790022005.

[13] Brian Maskew, Program VSAERO Theory Document. NASA Contractor Report 4023, September 1987.

[14] Bertagnolio, Franck. NACA0015 Measurements in LM Wind Tunnel and Turbulence Generated Noise. Report. Aeroelastic Design, Wind Energy Division, Risø National Laboratory for Sustainable Energy, Technical University of Denmark. Denmark.

[15] Kaufmann, Wick, and Wohlfahrt. "Airfoils for Fly Wings." Airfoils for Flying Wings and Tailless Airplanes. aerotools.de/airfoils/foil_flyingwings.htm.

[16] UrbanRail.net. UrbanRail.Net > Asia > Singapore > Singapore MRT (Metro). http://www.urbanrail.net/as/sing/singapore.htm.

[17] U.S. Standard Atmosphere, 1976. PDF. National Oceanic and Atmospheric Administration, National Aeronautics and Space Administration, United States Air Force, October 1976.

[18] G.U.N.T. Hamburg. "HM 170 Open wind tunnel. " https://www.gunt.de/en/products/open-wind-tunnel/070.17000/hm170/glct-1:pa-148:pr-769

[19] Alsoufi, Mohammad S., and Abdulrhman E. Elsayed. "Surface Roughness Quality and Dimensional Accuracy—A Comprehensive Analysis of 100% Infill Printed Parts Fabricated by a Personal/Desktop Cost-Effective FDM 3D Printer." Materials Sciences and Applications 09, no. 01 (2018): 11-40. doi:10.4236/msa.2018.91002.

[20] Morgado, J., R. Vizinho, M.a.r. Silvestre, and J.c. Páscoa. "XFOIL vs CFD performance predictions for high lift low Reynolds number airfoils." Aerospace Science and Technology 52 (2016): 207-14. doi:10.1016/j.ast.2016.02.031.

[21] MICROLIGHT WING GUIDE. PDF. Airborne Australia Pty Ltd.

[22] Young, T. M. "Aircraft Design Innovation: Creating an Environment for Creativity." Http://www.fzt.haw-hamburg.de/pers/Scholz/ewade/2005/JAERO2007_Young.pdf

[23] Spalart, P. R. and Allmaras, S. R., 1992, "A One-Equation Turbulence Model for Aerodynamic Flows" AIAA Paper 92-0439

[24] McCroskey, W. J. "A Critical Assessment of Wind Tunnel Results for the NACA 0012 Airfoil." NASA Technical Memorandum 100019, October 1987.

IX. APPENDIX

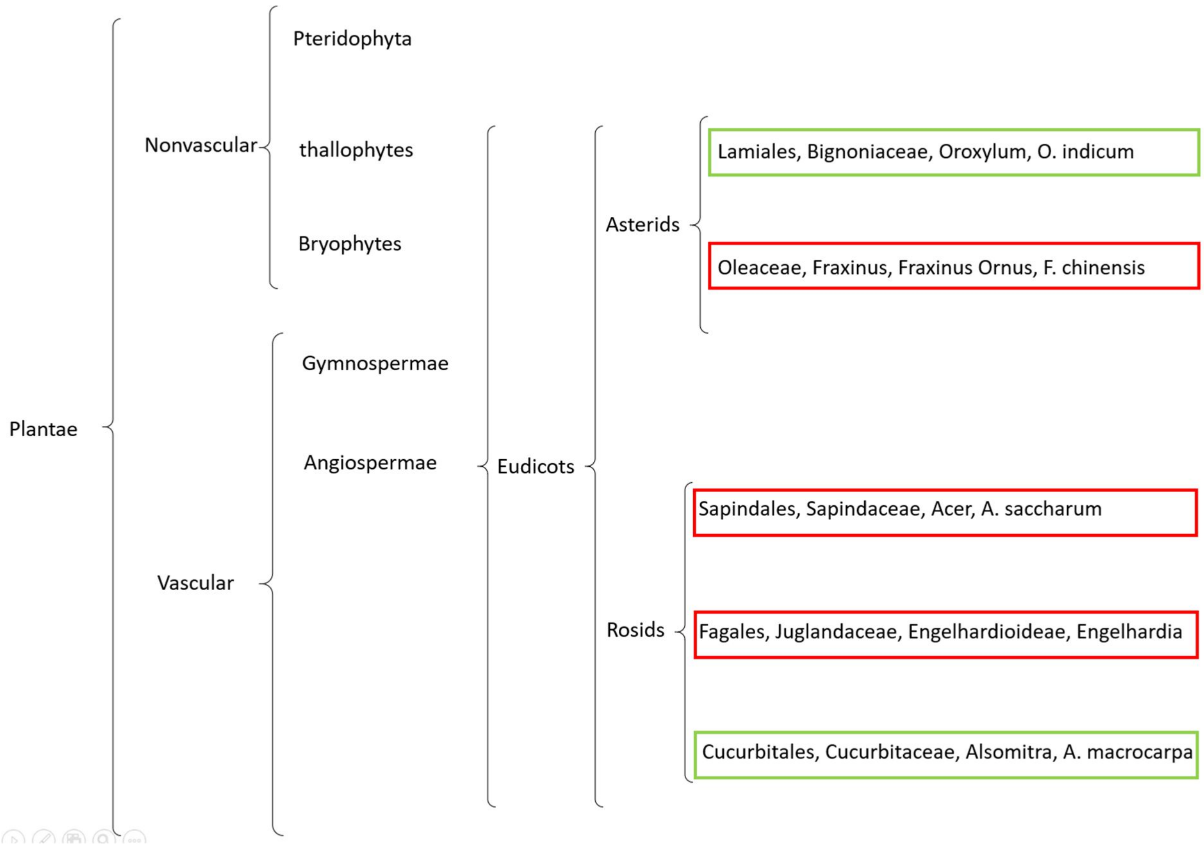

Figure 46. Seeds of the plants that can fly or glide.

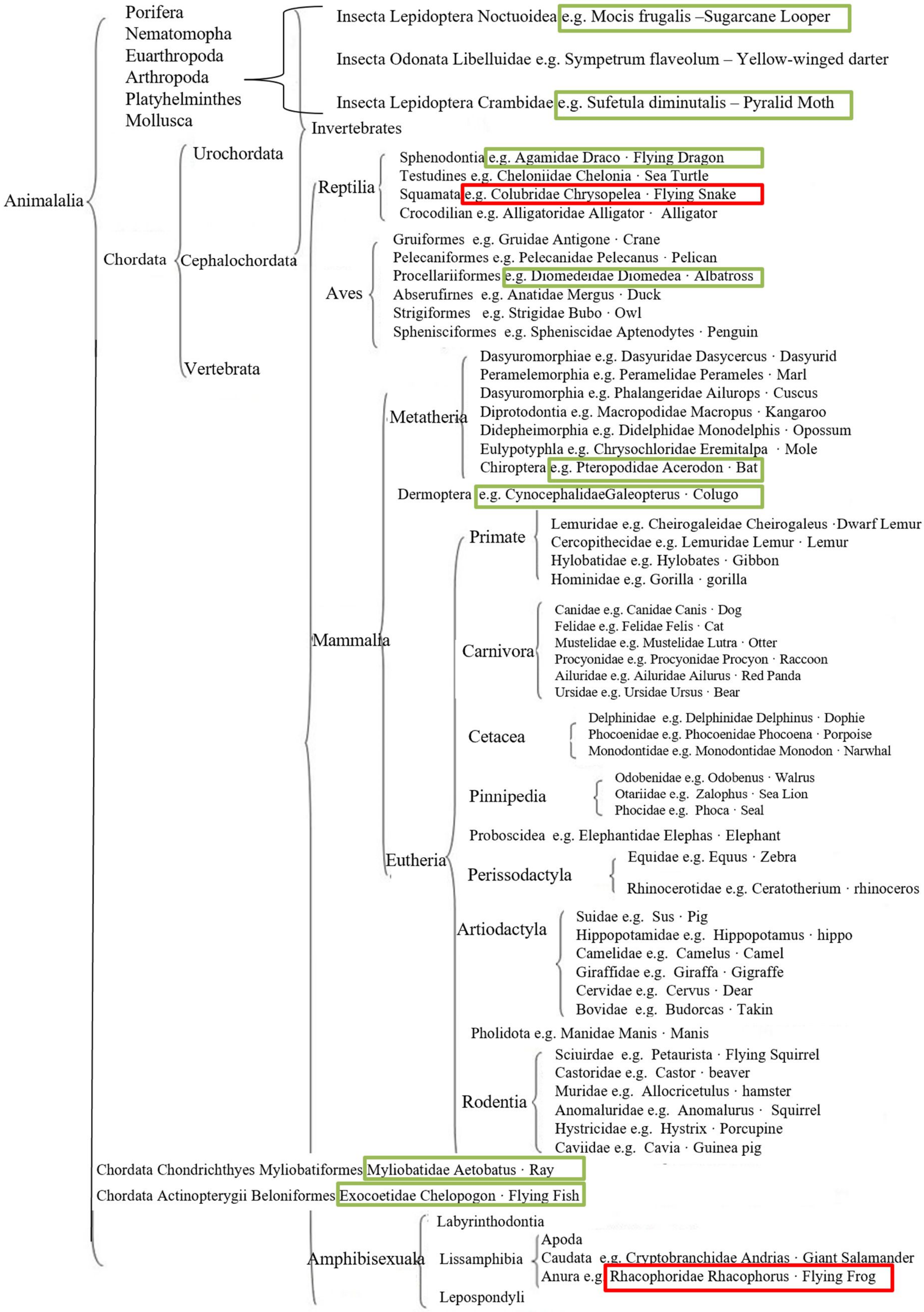

Figure 47. Animals that can fly or glide.